

# A Spectral Solver to Capture Unsteady Dynamics in the Aerospike Nozzle Wake

Zachary Pyle\* and Gustaaf B. Jacobs†

August 15, 2025

## Abstract

A robust, high fidelity spectral solver for supersonic and hypersonic flow over an aerospike nozzle is presented. Numerical stability is achieved with a novel hybrid artificial viscosity (AV) - finite volume subcell element (FVSE) shock capturing method. The AV method is computationally efficient. The diffusive FVSE method is locally called in elements where the AV method cannot sufficiently smooth the solution gradients, serving as a "parachute" in the context of numerical stability. The efficacy of this hybrid scheme is demonstrated on perfectly expanded Mach 2 and under expanded Mach 2 flow over a truncated aerospike and under expanded Mach 2 flow through a thruster module - aerospike nozzle assembly. The power spectral density of the unsteady pressure forcing on the nozzle is computed for each case and primary oscillation frequencies are identified. These oscillations are linked to flow patterns observed in Mach and schlieren images of the temporally evolving flow fields. To the authors' knowledge this is the first successful computation with a spectral solver of the unsteady, expanding, hypersonic flow over an aerospike from the initial thruster discharge until a quasi-steady state is achieved, as well as the first numerical investigation of the thruster module - aerospike nozzle assembly.

## Nomenclature

### Variables

$C_\kappa$	=	Scaling coefficient of numerical energy dissipation
$C_m$	=	Scaling coefficient of maximum numerical dissipation
$C_\mu$	=	Scaling coefficient of numerical momentum dissipation
$h$	=	Spike base height
$h_i$	=	Thruster module exit height
$M$	=	Mach number
$P$	=	Polynomial order of spectral elements
$p$	=	Pressure
$Re$	=	Reynolds number
$St$	=	Strouhal number
$t$	=	Time
$T$	=	Temperature
$U$	=	Velocity magnitude
$u$	=	Velocity in $x$ direction
$v$	=	Velocity in $y$ direction
$x_u$	=	Jet reattachment location

### Greek Letters

---

\*Doctoral Student, San Diego State University, Department of Aerospace Engineering, zpyle8687@sdsu.edu, AIAA Student Member

†Professor, San Diego State University, Department of Aerospace Engineering, gjacobs@sdsu.edu, Associate Fellow, Corresponding Author

$\alpha$	=	FVSE blending coefficient
$\kappa$	=	Thermal conductivity
$\mu$	=	Dynamic viscosity
$\rho$	=	Density
$\sigma$	=	Polynomial order of shock indicator function
$\tau$	=	Convective time unit
$\Psi$	=	Shock indicator
$\omega$	=	Vorticity
Subscripts		
$a$	=	Ambient
$e$	=	Thruster module exit plane
$f$	=	Reference
$h$	=	Artificial viscosity
$m$	=	Max
$o$	=	Stagnation
Abbreviations		
AV	=	Artificial viscosity
FVSE	=	Finite volume subcell element
MoC	=	Method of characteristics

## 1 Introduction

The revival of long-term space initiatives in both the public and private sectors has precipitated the development and maturation of nearly every aspect of launch vehicle technology. Complex fuel injector channels that mitigate pressure losses are now feasible through additive manufacturing. Rotating detonation chambers (RDCs) promise significant improvements in combustion efficiency. Advanced flight controllers opened the door to recoverable, reusable first stage boosters. Advances in material science have paved the way for lightweight, carbon-reinforced fairings and heat-resistant aluminum or titanium alloy skins. Even the fuel cycle of launch vehicles have improved; turbomachinery such as preburners and turbopumps are now used in full flow staged combustion cycles that produce larger specific impulses ( $I_{sp}$ ) than the pressure fed or gas generator cycles.

In stark contrast, the bell nozzle is still fundamentally the same converging-diverging nozzle that adorned the original V-2 rocket with the same inherent limitations to thrust efficiency. The expansion of an exhaust plume by a bell nozzle is restricted by the nozzle's area expansion ratio, thus the conversion of internal energy to kinetic energy by a bell nozzle is limited. In the context of launch vehicles this means bell nozzles achieve the maximum  $I_{sp}$ , or extract the maximum possible kinetic energy, at a single altitude. At this design altitude the static pressure of the exhaust plume is equivalent to the ambient pressure and the plume is axially aligned, minimizing losses within the nozzle flow and maximizing harnessed thrust. At lower altitudes shock diamonds form and generate losses, and at higher altitudes the flow is not purely axial and thrust is wasted.

A promising successor to the traditional bell nozzle is the altitude compensating aerospike nozzle. These nozzles perfectly expand the exhaust plume at all altitudes in a flight, increasing the energy extracted from the flow. The  $I_{sp}$  of the launch vehicle is increased throughout the flight envelope, with the most notable thrust increase occurring at altitudes below or at the design altitude where the exhaust plume is axially aligned [36, 25, 31, 38]. Additionally, the mechanically simple design of the aerospike minimizes avenues for structural failure. Manufacturing costs and launch turn-around time can be reduced by implementing an array of additively manufactured thruster modules about the aerospike (fig. 1), as discussed in [25, 24, 42].

The primary drawback of the aerospike nozzle is at low altitudes an oscillatory wake forms, inducing an unsteady pressure forcing on the nozzle that can degrade flight stability. Evidence of this was originally discovered in experimental investigations by Mueller et al. [38], Mueller et al. [39], and Mueller et al. [37].

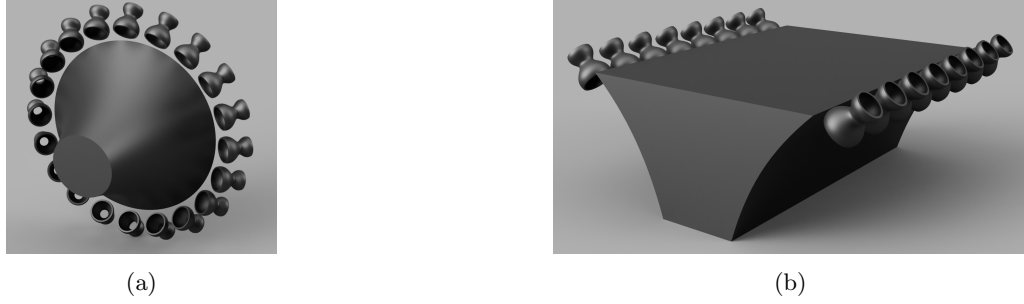


Figure 1: Modular (a) axisymmetric and (b) linear aerospike nozzle concepts. Individual thruster modules are manufactured separately and joined to the aerospike nozzle.

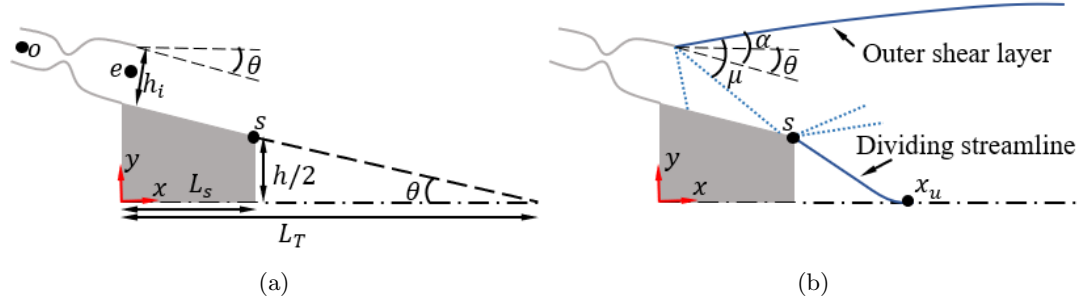


Figure 2: Schematic of under expanded flow over an aerospike nozzle in the closed wake regime. (a)  $L_T$  and  $L_s$  are the non truncated and truncated spike lengths,  $h$  is the spike base height,  $h_i$  is the thruster module height measured normal to the ramp, and  $\theta$  is the ramp angle. (b)  $\alpha$  is the flow deflection angle through the thruster expansion fan,  $\mu$  is the Prandtl-Meyer expansion fan angle, and  $x_u$  is the jet impingement point.

In these investigations a distinct transition in wake dynamics was observed as the nozzle pressure ratio, or the ratio of the combustion chamber pressure to the ambient pressure ( $p_o/p_a$ ) was increased. The low altitude regime was classified as an "open wake" and the high altitude regime was classified as a "closed wake". Later spectral analyses of the integrated pressure signal along the spike walls and spike base in the open wake regime by Verma et al. [63] revealed an unsteady pressure forcing that exhibited a clear primary frequency.

Computational investigations into the driving mechanism of the oscillatory aerospike wake have historically relied on steady state flow models and dissipative finite volume solvers to ensure numerical stability. Investigations by Hagemann et al. [23, 25, 24] into the steady, inviscid aerospike wake revealed that wake closure occurs when characteristics generated at the thruster module expansion fan do not impinging on the streamline dividing the supersonic jets and the subsonic recirculation region (fig. 2), which hints towards a coupling mechanism between the dividing streamline and the outer shear layer. This is further supported by RANS model and method of characteristics investigations by Pyle et al. in which wake closure is observed as a function of the inviscid jet height to spike base ratio,  $h_i/h$  (fig. 2) as opposed to pressure ratio. Pyle et al. [48] shows changing  $h_i/h$  alters the expansion - compression wave pattern observed in the inviscid jet that impinge on the dividing streamline between the inviscid jet and viscous recirculation region. Other notable experimental and RANS model investigation are those by Chutkey et al. [13, 14, 15], Nair et al. [40, 41], and Soman et al. [56]. Most recently Golliard and Mihaescu [21] investigated the unsteady, three dimensional wake, however dissipative second order finite volume scheme was used to maintain a numerically stable solution.

To discern the driving mechanism behind the wake oscillations and resolve the unsteady pressure forcing on the aerospike nozzle high fidelity computations of the unsteady flow field are required. An increasingly popular choice of solver for such computations are discontinuous Galerkin spectral element

method (DGSEM) solvers; their low dissipation and dispersion errors make them excellent candidates for LES and DNS of smooth flows and the investigation of unsteady flows and instabilities. [30, 57, 53, 2, 33, 52, 51]. As this method is local (per element) parallelization is efficient and results in a near linear scaling of computational cost. Additionally, a judicious choice of numerical fluxes may ensure the numerical scheme preserves kinetic energy preserving, improving numerical stability of even marginally solved solutions [34, 28].

A major challenge in computing unsteady supersonic or hypersonic flows such as the aerospoke nozzle using a DGSEM solver is maintaining numerical stability in the presence of shock waves. Approximating the solution across the sharp gradients introduces numerical oscillations, potentially incurring non-physical negative densities, pressures, and temperatures. Various shock capturing schemes have been proposed to address this, such as weighted essentially non-oscillatory (WENO) schemes [54, 17], slope limiters [16, 19], artificial viscosity (AV)[5, 65, 1, 10], and hybrid spectral element - finite volume subcell element (FVSE) schemes [27]. Recent investigations into the accuracy and stability of shock capturing schemes applied to hypersonic flows by Peck et al. [44] show FVSE schemes provide a greater improvement to numerical stability than slope limiters or AV schemes with comparable degradation of global accuracy.

In this paper we present a robust DGSEM solver capable of computing the unsteady supersonic and hypersonic wake downstream of a modular aerospoke nozzle. This is enabled by a hybridized artificial viscosity (AV) - finite volume subcell element (FVSE) shock capturing scheme. The AV method is the primary scheme and the FVSE method is called locally in elements where the artificial viscosity exceeds a proscribed threshold, serving as a "numerical parachute". First, we offer a brief description of the governing equations, corresponding numerical approximations, and the hybridized shock capturing scheme. Then grid requirements, tuning of the shock capturing method, and initial and boundary conditions are discussed. Finally a systematic development of test cases is presented: first, perfectly expanded Mach 2 flow over an aerospoke nozzle in which the computational domain is truncated downstream of the thruster modules, then under expanded Mach 2 flow over an aerospoke nozzle without thruster modules, and finally under expanded Mach 2 flow over though a thruster module - aerospoke nozzle assembly. An investigation into the proper tuning coefficients of the hybrid shock capturing scheme to avoid over dissipation is presented in the perfectly expanded Mach 2 case. The efficacy and general applicability of those tuning coefficients to progressively harsher initial conditions and complex geometries is demonstrated in the under expanded Mach 2 cases. Primary frequencies of the unsteady pressure forcing on the nozzle are extracted and presented in each test case. To the authors' knowledge this is the first instance the thruster module - aerospoke nozzle configuration has been investigated and stable, spectrally accurate results of the unsteady hypersonic wake has been presented.

## 2 Governing Equations

The non-dimensional Navier-Stokes equations governing compressible flow may be cast as

$$\mathbf{Q}_t + \nabla \cdot \mathcal{F} = 0 \quad (1)$$

where  $\mathbf{Q}$  is the solution vector, defined as

$$\mathbf{Q} = [\rho \quad \rho u \quad \rho v \quad \rho w \quad \rho E]^T, \quad (2)$$

and  $\mathcal{F}$  is the flux matrix, defined as

$$\mathcal{F} = [\mathbf{F}, \mathbf{G}, \mathbf{H}].$$

$\mathbf{F}, \mathbf{G}, \mathbf{H}$  are the flux vectors in the  $x, y, z$  directions. The flux vectors may be further decomposed into advective and viscous fluxes:

$$\mathbf{F} = \mathbf{F}^a + \frac{1}{Re_f} \mathbf{F}^v, \quad \mathbf{G} = \mathbf{G}^a + \frac{1}{Re_f} \mathbf{G}^v, \quad \mathbf{H} = \mathbf{H}^a + \frac{1}{Re_f} \mathbf{H}^v.$$



The superscripts  $a$  and  $v$  denote advective and viscous fluxes. The advective and viscous fluxes are defined as

$$\begin{aligned}\mathbf{F}^a &= [\rho u \quad \rho u u + p \quad \rho v u \quad \rho w u \quad u(\rho E + p)]^T, \\ \mathbf{G}^a &= [\rho v \quad \rho u v \quad \rho v v + p \quad \rho w v \quad v(\rho E + p)]^T, \\ \mathbf{H}^a &= [\rho w \quad \rho u w \quad \rho v w \quad \rho w w + p \quad w(\rho E + p)]^T,\end{aligned}\tag{3}$$

$$\begin{aligned}\mathbf{F}^v &= \left[0 \quad \tau_{xx} \quad \tau_{yx} \quad \tau_{zx} \quad u\tau_{xx} + v\tau_{yx} + z\tau_{zx} + \frac{T_x}{(\gamma-1)Pr_f M_f^2}\right]^T, \\ \mathbf{G}^v &= \left[0 \quad \tau_{xy} \quad \tau_{yy} \quad \tau_{zy} \quad u\tau_{xy} + v\tau_{yy} + z\tau_{zy} + \frac{T_y}{(\gamma-1)Pr_f M_f^2}\right]^T, \\ \mathbf{H}^v &= \left[0 \quad \tau_{xz} \quad \tau_{yz} \quad \tau_{zz} \quad u\tau_{xz} + v\tau_{yz} + z\tau_{zz} + \frac{T_z}{(\gamma-1)Pr_f M_f^2}\right]^T.\end{aligned}\tag{4}$$

$\rho E$  is the sum of the internal energy and kinetic energy per unit volume, given by

$$\rho E = \frac{p}{\gamma - 1} + \frac{\rho}{2}(u^2 + v^2 + w^2),\tag{5}$$

and  $\tau$  is the shear stress tensor. The system of equations is closed by the equation of state

$$p = \frac{\rho T}{\gamma M_f^2}.\tag{6}$$

$Re_f$ ,  $Pr_f$ , and  $M_f$  are the reference Reynolds, Prandtl, and Mach numbers defined as:

$$Re_f = \frac{\rho_f U_f L}{\mu(T_f)}\tag{7}$$

$$Pr_f = \frac{\mu(R - C_v)}{\kappa}\tag{8}$$

$$M_f = \frac{U_f}{\sqrt{\gamma R T_f}}\tag{9}$$

### 3 Numerical Methods

In this section a brief description of split form discontinuous Galerkin approximation is discussed. We outline the artificial viscosity shock capturing method and the Finite Volume Subcell Element (FVSE) shock capturing method. For generality all discussion in this section will refer to three dimensional geometries, however all results presented are two dimensional.

#### 3.1 Discontinuous Galerkin Spectral Element Method (DGSEM)

The physical domain that Equation (1) is approximated over is divided into  $E$  Elements,  $\Omega_e$ ,  $e = 1, 2, \dots, E$ . Each element is mapped from the physical domain,  $\mathcal{R}^3$ , to a unit cube computational domain,  $\tilde{\Omega}_e \in [0, 1]^3$  via an iso-parametric mapping  $\mathbf{x} = \mathbf{X}(\xi, \eta, \zeta)$ . Under this transformation (1) is rewritten as

$$\tilde{\mathbf{Q}}_t + \nabla_\xi \cdot \tilde{\mathcal{F}} = 0.\tag{10}$$

The tilde,  $\tilde{\phantom{x}}$ , denotes mapped quantities and  $\nabla_\xi = \frac{\partial}{\partial \xi} + \frac{\partial}{\partial \eta} + \frac{\partial}{\partial \zeta}$ .  $\tilde{\mathbf{Q}}$  is related to  $\mathbf{Q}$  via

$$\tilde{\mathbf{Q}} = J\mathbf{Q},\tag{11}$$

where  $J$  is the determinant of the Jacobian matrix:

$$\mathbf{J} = \begin{bmatrix} \frac{\partial x}{\partial \xi} & \frac{\partial x}{\partial \eta} & \frac{\partial x}{\partial \zeta} \\ \frac{\partial y}{\partial \xi} & \frac{\partial y}{\partial \eta} & \frac{\partial y}{\partial \zeta} \\ \frac{\partial z}{\partial \xi} & \frac{\partial z}{\partial \eta} & \frac{\partial z}{\partial \zeta} \end{bmatrix} = \begin{bmatrix} x_\xi & x_\eta & x_\zeta \\ y_\xi & y_\eta & y_\zeta \\ z_\xi & z_\eta & z_\zeta \end{bmatrix},$$

$$J = ||\mathbf{J}|| = x_\xi(y_\eta z_\zeta - y_\zeta z_\eta) - x_\eta(y_\xi z_\zeta - y_\zeta z_\xi) + x_\zeta(y_\xi z_\eta - y_\eta z_\xi).$$

$\tilde{\mathcal{F}}$  is defined as

$$\tilde{\mathcal{F}} = [\tilde{\mathbf{F}}, \tilde{\mathbf{G}}, \tilde{\mathbf{H}}], \quad (12)$$

where  $\tilde{\mathbf{F}}, \tilde{\mathbf{G}}, \tilde{\mathbf{H}}$  are the contravariant fluxes. The solution vector and contravariant fluxes in (10) are approximated as  $p^{th}$  order polynomials:

$$\tilde{\mathbf{Q}}_t(\xi, \eta, \zeta, t) \approx \tilde{\mathbf{Q}}^p(\xi, \eta, \zeta, t) = \sum_{i=0}^p \sum_{j=0}^p \sum_{k=0}^p \mathbf{Q}_{ijk}^p(t) \ell_i(\xi) \ell_j(\eta) \ell_k(\zeta), \quad (13)$$

$$\begin{aligned} \tilde{\mathbf{F}}(\xi, \eta, \zeta, t) &\approx \tilde{\mathbf{F}}^p(\xi, \eta, \zeta, t) = \sum_{i=0}^p \sum_{j=0}^p \sum_{k=0}^p \mathbf{F}_{ijk}^p(t) \ell_i(\xi) \ell_j(\eta) \ell_k(\zeta), \\ \tilde{\mathbf{G}}(\xi, \eta, \zeta, t) &\approx \tilde{\mathbf{G}}^p(\xi, \eta, \zeta, t) = \sum_{i=0}^p \sum_{j=0}^p \sum_{k=0}^p \mathbf{G}_{ijk}^p(t) \ell_i(\xi) \ell_j(\eta) \ell_k(\zeta), \\ \tilde{\mathbf{H}}(\xi, \eta, \zeta, t) &\approx \tilde{\mathbf{H}}^p(\xi, \eta, \zeta, t) = \sum_{i=0}^p \sum_{j=0}^p \sum_{k=0}^p \mathbf{H}_{ijk}^p(t) \ell_i(\xi) \ell_j(\eta) \ell_k(\zeta). \end{aligned} \quad (14)$$

In equations (13) and (14)  $\ell$  is the Lagrange polynomial:

$$\ell_i(x) = \prod_{\substack{n=0 \\ n \neq i}}^N \frac{x - x_n}{x_i - x_n}. \quad (15)$$

Substituting (13) and (14) into (10) yields

$$\tilde{\mathbf{Q}}_t^p + \nabla_\xi \cdot \tilde{\mathcal{F}}^p = 0. \quad (16)$$

The flux divergence is computed via

$$\begin{aligned} \nabla_\xi \cdot \tilde{\mathcal{F}} &= \tilde{\mathbf{F}}_\xi + \tilde{\mathbf{G}}_\eta + \tilde{\mathbf{H}}_\zeta \\ &= D_\xi \tilde{\mathbf{F}} + D_\eta \tilde{\mathbf{G}} + D_\zeta \tilde{\mathbf{H}}, \end{aligned}$$

where  $D_\xi, D_\eta, D_\zeta$  are the polynomial derivative matrices in the  $\xi, \eta, \zeta$  directions respectively.

For the detailed derivation of the DGSEM approximation we refer to [35, 20], and for the derivation of the split-form approximation we refer to [34]. The end result is the strong form of the equations:

$$\int_\Omega \phi^T \tilde{\mathbf{Q}}_t d\Omega + \int_\Gamma \phi^T (\tilde{\mathcal{F}}^* - \tilde{\mathcal{F}}) \cdot \hat{n} d\Gamma + \int_\Omega \phi^T (\nabla \cdot \tilde{\mathcal{F}}) d\Omega = 0. \quad (17)$$

where  $*$  denotes a numerical flux, and the volumetric flux terms are represented by the two-point kinetic energy preserving Pirozzoli fluxes [46].  $\tilde{\mathbf{Q}}_t$  is integrated using a fourth order Runge-Kutta scheme with a  $CFL$  number of 0.1 in all presented cases.

### 3.2 Artificial Viscosity Shock Capturing Scheme (SV)

In the artificial viscosity (AV) method a numerical dissipation term is introduced to the DG approximation that smooths the solution. If properly coupled to a shock sensor, this smoothing occurs only in the presence of sharp gradients. The chosen AV method is the entropy - generation based method detailed by Chaudhuri et al. in [10, 9, 8].

The physical viscosity and thermal conductivity terms,  $\mu$  and  $\kappa$  in (4), are augmented as follows:

$$\begin{aligned}\mu_t &= \hat{\mu}_h Re_f + \mu \\ \kappa_t &= \hat{\kappa}_h Re_f + \kappa.\end{aligned}\tag{18}$$

$\mu_h$  and  $\kappa_h$  are the artificial viscosity and thermal conductivity terms, defined as

$$\begin{aligned}\mu_h &= \hat{\mu}_h \theta \mathcal{H}(-\nabla \cdot \tilde{\mathbf{u}}), \\ \kappa_h &= \hat{\kappa}_h \theta,\end{aligned}\tag{19}$$

where  $\mathcal{H}$  is the Heaviside step function.  $\hat{\mu}$  and  $\hat{\kappa}$  are computed according to:

$$\begin{aligned}\hat{\mu}_h &= C_\mu \frac{\rho(\Delta h)^2}{\|\rho s - \bar{\rho} \bar{s}\|_\infty} \left[ \frac{\Phi}{T} \right], \\ \hat{\kappa}_h &= C_\kappa \frac{\rho(\Delta h)^2}{\|\rho s - \bar{\rho} \bar{s}\|_\infty} \left[ \frac{\Gamma}{Pr_f T(\gamma - 1) M_f^2} \right].\end{aligned}\tag{20}$$

$\Phi$  and  $\Gamma$  are the non-dimensional viscous and conductive entropy generation respectively.  $\|\rho s - \bar{\rho} \bar{s}\|_\infty$  is the modulus of the entropy norm, and  $C_\mu, C_\kappa$  are tuning coefficients.  $\Delta h$  is the minimum nodal spacing within an element. Under this formulation the numerical dissipation terms approach 0 in isentropic and grid resolved flows. For the full derivation of Equation (20) we refer to [10].

To avoid over-dissipation in regions of both high entropy generation and physical viscosity (e.g. boundary and shear layers) a so-called Ducros sensor [18, 45, 10] is formulated:

$$\theta = \frac{(\nabla \cdot \tilde{\mathbf{u}})^2}{(\nabla \cdot \tilde{\mathbf{u}})^2 + (\nabla \times \tilde{\mathbf{u}})^2 + \epsilon},\tag{21}$$

Near shocks  $\theta \rightarrow 1$  and in regions dominated by shear or rotational flow  $\theta \rightarrow 0$ . In equation (21),  $\epsilon = 10^{-12}$ , ensuring division by zero never occurs.

A major drawback of the artificial viscosity method when used in conjunction with an explicit time integration scheme is the constraint it imposes on the viscous time step. As the artificial viscosity is increased to stabilize the flow the viscous time step, defined as

$$\Delta t_v = CFL_v Re_f \frac{(\Delta h)^2}{\nu + \nu_h},\tag{22}$$

may become prohibitively small. To mitigate this a restriction is placed on the artificial viscosity:

$$\mu_{max} = C_m \rho \Delta h (\|\mathbf{u}\| + \sqrt{T})\tag{23}$$

where  $C_m$  is a modeling parameter. Limiting the artificial viscosity in this manner trades the stability of large  $\mu_h$  values for a feasible time step.

It is worth mentioning that no analytical bounds on  $(C_\mu, C_\kappa, C_m)$  that ensure numerical stability have been derived; this is one of the major short comings of artificial viscosity based shock capturing schemes, as discussed by Chaudhuri et al. [10] and later Peck et al. [44]. These design parameters are highly case dependent and as we see in Equation (20)  $\hat{\mu}$  and  $\hat{\kappa}$  are functions of temperature, grid size, and entropy generation.

### 3.3 Finite Volume Subcell Element Shock Capturing Scheme (FVSE)

In the FVSE method the high order DGSEM solution is blended with a low order finite volume solution at each node within the element [27]. By choosing the highly dissipative Lax-Friedrichs method to compute the numerical flux between each subcell the finite volume solution is probably monotonic. This does incur the additional computational cost of calling a Riemann solver between every node within a DG element, however blending the DG and FVSE solutions greatly improves the numerical stability of the solver. Blending is computed according to

$$\begin{aligned} (\tilde{\mathbf{Q}}_t)_{ijk} &= -\nabla_\xi \cdot \tilde{\mathcal{F}}_{ijk} = \mathcal{R}_{ijk} \\ &= \alpha \mathcal{R}_{ijk}^{FVSE} + (1 - \alpha) \mathcal{R}_{ijk}^{DGSEM}. \end{aligned} \quad (24)$$

$\mathcal{R}_{ijk}^{DGSEM}$  is computed according to Equation (17) at the quadrature node  $ijk$  within an element.  $\mathcal{R}_{ijk}^{FVSE}$  is defined according to the chosen finite volume scheme at the quadrature node  $ijk$  within an element. By blending the DG and FVSE solution element-wise rather than node-wise local conservation is maintained [27]. For the full derivation of  $\mathcal{R}_{ijk}^{FVSE}$  we refer to [27].

To maintain global higher-order accuracy of the solution the blending coefficient,  $\alpha$ , in Equation (24) is computed on a per-element basis each time Runge-Kutta step as follows:

$$\alpha = \begin{cases} \alpha_{min} & , \quad \tilde{\alpha} < \alpha_{min} \\ \tilde{\alpha} & , \quad \alpha_{min} \leq \tilde{\alpha} \leq \alpha_{max} \\ \alpha_{max} & , \quad \tilde{\alpha} > \alpha_{max} \end{cases} \quad (25)$$

where  $\tilde{\alpha}$  is defined as

$$\tilde{\alpha} = \Psi^\sigma + \alpha_{min}. \quad (26)$$

Here  $\Psi$  is a shock indicator that ranges from 0 to 1 and  $\sigma$  is an integer in the range  $[1, \infty]$ . In all cases  $\alpha_{max} = 1$ ,  $\alpha_{min} = 0$ .

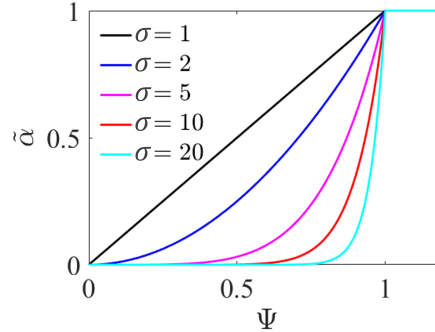


Figure 3: The FVSE blending coefficient,  $\tilde{\alpha}$ , as a function of the shock sensor,  $\Psi$  (eq. 26).

### 3.4 The Hybrid Shock Capturing Scheme

To capitalize on the cost effective, accuracy preserving AV method and the highly robust FVSE method we implement a hybridized shock capturing scheme. The entropy - generation based AV method is the primary scheme, ensure numerical dissipation is not introduced in smooth, isentropic, or grid resolved regions of the flow. The FVSE is treated as a "parachute", called in elements where the AV method does not sufficiently smooth the flow. To achieve this the shock sensor  $\Psi$  (26) is defined as:

$$\Psi = \frac{\max(\hat{\mu}_h, \hat{\kappa}_h)}{\mu_{max}} \quad (27)$$

This accrues no additional overhead when computing the shock sensor and seamlessly integrates the AV and FVSE method compared to other popular shock sensor choices such as a Persson sensor, gradient sensor, or jump sensor. However this choice in  $\Psi$  means the blending coefficient,  $\alpha$ , can be indirectly influenced by the AV coefficients,  $(C_\mu, C_\kappa, C_m)$ , through the computation of  $\hat{\mu}_h$  (20) and  $\hat{\mu}_{max}$  (23). We have found stable results without excessive dissipation by enforcing  $(C_\mu, C_\kappa, C_m) = (0.5, 0.5, 0.5)$  in all cases; this aligns with the suggested values by Chaudhuri et al. when developing the AV method. Decreasing the AV coefficients both reduces the artificial viscosity and decreases  $\alpha$ , reducing numerical stability. Conversely increasing the AV coefficients increases the artificial viscosity and increases  $\alpha$ , overly dissipating the solution.

## 4 Computational Model

The solver is applied to three cases: perfectly expanded Mach 2 flow and under expanded Mach 2 flow over an linear, truncated, aerospike nozzle and under expanded Mach 2 flow through a thruster module - aerospike nozzle assembly. The initial and boundary conditions of each case are presented and non-dimensional inlet, outlet, stagnation, and reference values are tabulated. The hybrid AV - FVSE shock capturing scheme requires minimal tuning between each case. All test cases require special treatment at the sharp spike tip corners to remain numerically stable.

### 4.1 Perfectly Expanded Mach 2 Jets

We first consider the perfectly expanded, Mach 2 jet flow over a linear, truncated, conical (non-contoured), aerospike nozzle in quiescent air at sea level. This aerospike geometry is representative of a space plane propulsion system, for example POLARIS's MIRA and MIRA II vehicles [43, 58], and both experimental and RANS model investigations of this configuration are readily available to draw from [23, 25, 24, 13, 12, 62, 61, 56, 32, 48]. A conical design mitigates centrifugal instabilities such as Gortler vortices along the ramp, allowing the fundamental behavior of the wall bounded jets and wake stability to be investigated. An inclination angle of  $\theta = 15^\circ$  is chosen so results may be compared to previous computational and experimental investigations [61, 56, 48]. The spike truncation percentage, defined as

$$\chi = \frac{L_s}{L_s + h/(2\tan(\theta))} \times 100\%, \quad (28)$$

is  $\chi = 38.5\%$ .  $h, L_s, \theta, L_T$  are defined in Figure 2a.

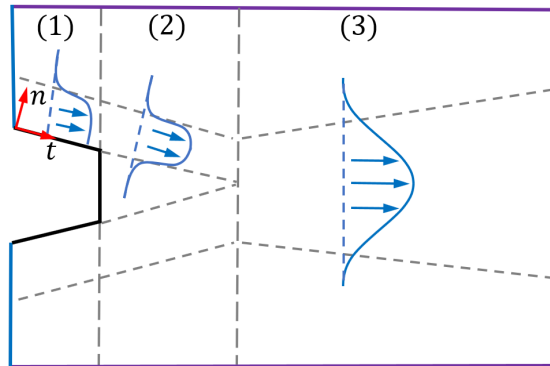


Figure 4: The computational domain of the perfectly expanded Mach 2 case. Inlet, outlet, and slip wall conditions are demarcated by blue, purple, and black lines respectively. The velocity field is initialized with a single hyperbolic tangent, double hyperbolic tangent, and turbulent jet profiles are illustrated in sections (1), (2), and (3) respectively.

Perfectly expanded jets are implemented so shear instabilities along the outer shear layer (fig. 2b) may be studied independent of screech tones or Mach waves found in over and under expanded jets. Screech tones have been shown to excite shear instabilities in jets [60, 59] and enhance individual modes which can

obscure the dominant frequencies of the non-excited wake [21]. Expansion - compression cells formed by rebounding Mach waves may lead to flow separation or coalesce into oblique shocks, as demonstrated by Pyle et al. [48].

All spike walls are treated as slip walls, primarily to reduce computational cost that accompanies resolving the boundary layer. Based on work by Zhuang and Dimotakis [66] we expect the absence of the boundary layer momentum deficit to have a slight stabilizing effect on the shear layer separating the supersonic jet and the base recirculation region. Zhuang and Dimotakis found such a deficit introduces a so-called "wake mode" to shear layer, however the maximum growth rate of the wake mode is an order of magnitude smaller than the "weak supersonic" and "strong supersonic" modes observed in both the boundary layer impacted and non-impacted mixing layers.

To further lower the computational cost the thruster module is not included in the simulated domain (fig. 4). Chai et al. [7, 32]. found the accuracy of the mean flow field to be unaffected by such a domain truncation if the inlet profiles imposed on the reduced domain are extracted from the non-reduced domain. Further investigations by Pyle et al. [48] found the inlet state variable profiles may instead be analytically computed according to the isentropic flow equations while still maintaining accuracy:

$$\begin{aligned}\frac{T_o}{T} &= 1 + \frac{\gamma - 1}{2} M^2, \\ \frac{\rho_o}{\rho} &= \left(1 + \frac{\gamma - 1}{2} M^2\right)^{\frac{1}{\gamma - 1}}, \\ \frac{p_o}{p} &= \left(1 + \frac{\gamma - 1}{2} M^2\right)^{\frac{\gamma}{\gamma - 1}}.\end{aligned}\tag{29}$$

The truncated domain spans the region  $y \in [-5, 5]$ ,  $x \in [0, 17]$ , chosen for computationally feasibility.

A Mach 2 jet profile is imposed at the inlet of the truncated computational domain. This Mach number is chosen to avoid the suppression of shear and wake instabilities that is reported at higher Mach numbers by Ragab and Wu [49], Bashkin et al. [6], and Harris and Fasel [26]. Additionally, Mach numbers in the range 2 – 2.5 are commonly seen in experimental aerospike nozzle investigations [63, 62, 61, 64, 55] as the large pressure ratio required to achieve higher Mach numbers is difficult to achieve without reducing the ambient static pressure via parallel flow. Thus, this configuration is relevant to both the experimental and computational community. The resulting static jet pressure, density, and temperature at the inlet are equivalent to the ambient pressure, density, and temperature:  $p_a, \rho_a, T_a$ . Ambient conditions are enforced at the outlets.

The flow is initialized as two impinging jets (fig. 4) with three distinct sections: (1) jet flow over a slip wall, (2) jet flow bounding a viscous recirculation region, (3) a fully developed turbulent jet. Section (1) spans  $x \in [0, L_s]$ . The velocity is computed according to

$$\mathbf{u} = \begin{bmatrix} u \\ v \end{bmatrix} = \begin{bmatrix} f(n) \cos(\theta) U \\ f(n) \frac{|y|}{y} \sin(\theta) U \end{bmatrix}.\tag{30}$$

Here  $U$  is the non-dimensional velocity magnitude of the supersonic jet computed via the jet Mach number at the thruster exit,  $M_e$ , and isentropic temperature equation (eq. 29). The  $-\frac{|y|}{y}$  factor ensures the sign of  $v$  is correctly assigned.  $f(n)$  is the shape function

$$f(n) = -\frac{1}{2} [\tanh(\gamma(\frac{n}{h_i} - 1)) - 1].\tag{31}$$

The hyperbolic tangent profile models the outer shear layer and the slip wall condition.  $n$  is the normal coordinate with respect to the spike ramp (fig. 4). The  $\mathcal{R}\epsilon[x - y] \rightarrow \mathcal{R}\epsilon[t - n]$  mapping is computed according to:

$$t(x) = \frac{x}{L_s},\tag{32}$$

$$y_w(t) = \frac{h}{2} + L_s \tan(\theta)(1 - t), \quad (33)$$

$$n(t, y) = (|y| - y_w(t)) \cos(\theta). \quad (34)$$

Section (2) spans  $x \in [L_s, x_u]$ , where  $x_u$  is the predicted impingement point of the jet on the  $y = 0$  axis (fig. 2b), computed by solving Equation (33) for  $y_w(t) = 0$  and inverting the  $x \rightarrow t$  mapping (eq. (32)). A new shape function is applied to Equation (30)

$$g(n) = g_1(n) + g_2(n), \quad (35)$$

where  $g_1(n)$  and  $g_2(n)$  are defined as

$$g_1(n) = f(n) = -\frac{1}{2}[\tanh(\gamma(\frac{n}{h_i} - 1)) - 1], \quad (36)$$

$$g_2(n) = \frac{1}{2}[\tanh(\gamma(\frac{n}{h_i})) - 1]. \quad (37)$$

This dual hyperbolic tangent profile models the inner and outer shear layers (fig. 2). Similar to section (1), the velocity is computed as

$$\mathbf{u} = \begin{bmatrix} u \\ v \end{bmatrix} = \begin{bmatrix} g(n) \cos(\theta)U \\ g(n) \frac{|y|}{y} \sin(\theta)U \end{bmatrix}. \quad (38)$$

The shape profile in section (3) is computed according to a fully developed turbulent planar jet velocity profile

$$h(\tilde{\eta}) = \text{sech}^2(\psi \tilde{\eta}), \quad (39)$$

where  $\tilde{\eta} = \frac{y}{y_{1/2}(x)}$  and  $\psi = \frac{1}{2} \ln(1 + \sqrt{2})^2$ . We refer to Chapter 5 in the text book by Pope, [47], for details of how the constant  $\psi$  is obtained and the exact dependency of  $y_{1/2}$  on  $x$ .

The  $x - y$  coordinate system is used in Equation (39) rather than the  $t - n$  system because the flow is assumed to be axially aligned. The velocity is computed as

$$\mathbf{u} = \begin{bmatrix} u \\ v \end{bmatrix} = \begin{bmatrix} h(\tilde{\eta})U \\ 0 \end{bmatrix}. \quad (40)$$

The reference values used to non-dimensionalize the flow are computed according to Table 1. The reference, inlet, ambient, and stagnation variables are listed in Table 2; "e" refers to values at the thruster exit, computed via the isentropic flow equations (eq. (29)). "f" refers to reference variables, "a" refers to ambient variables, and "o" refers to stagnation variables. Under these conditions the reference Reynolds number is  $Re_f = 95,000$ . According experimental and computational investigations by Grasso and Pettinelli [22] and later Hinman and Johansen [29] into supersonic and hypersonic wakes we expect both linear and non-linear instabilities to occur at this Mach and Reynolds number. Increasing the Reynolds number further increases the scale separation rather than introducing new instabilities.

$M_f$	$\rho_f$	$U_f$	$T_f$	$p_f$	$L_f$	$\tau_f$	$Re_f$
1	$\rho_e$	$U_e$	$(\frac{U_e M_f}{M_e})^2$	$\rho_e U_e U_e$	$h$	$L_f / U_f$	$\frac{\rho_f U_f L_f}{\mu(T_f)}$

Table 1: The formulation of reference variables used to non-dimensionalize the Navier-Stokes equations. "e" denotes values extracted at the thruster exit plane (fig. 2a).

To ensure numerical stability over the sharp spike corners the FVSE blending coefficient,  $\alpha$ , is explicitly assigned as

$$\alpha = \begin{cases} \sqrt{(x - x_c)^2 + (y - y_c)^2} < R, & 1 \\ \sqrt{(x - x_c)^2 + (y - y_c)^2} > R, & \alpha \end{cases}. \quad (41)$$

	$\rho$	$U$	$T$	$p$	$M$
<i>o</i>	4.35	0	0.45	1.40	0
<i>e</i>	1	1	0.25	0.18	2
<i>a</i>	1	0	0.25	0.18	0
<i>f</i>	1.24 [kg/m <sup>3</sup> ]	676 [m/s]	1137 [K]	576,288 [Pa]	1

Table 2: Non-dimensional values used in the perfectly expanded Mach 2 jets case. Points "o", "e", and "a" are found in the combustion chamber, at the thruster exit, and in the ambient respectively. "f" indicates the reference values.

$x_c, y_c$  are the coordinates of the spike corners, and  $R$  is a prescribed radius of  $R = 0.0125$ ; this is the smallest radius tested that maintains numerical stability. This explicit assignment necessary because Prandtl-Meyer fans form at spike corners, leading to undershoots in the pressure, density, and temperature approximations. Because flow through the expansion fans are isentropic  $\hat{\mu}_h \rightarrow 0$  and neither the AV nor the FVSE methods are triggered. Because the Lax-Friedrichs fluxes used in the FVSE method are monotonic enforcing an  $\alpha = 1$  region about the spike corners eliminates these undershoots and ensures stability.

To prevent spurious boundary reflections a dissipative damping layer is imposed over the region  $x \in [15, 17], y \in [3, 5]$ . In the range  $x \in [15, 16], y \in [3, 4]$   $\alpha$  is increased linearly to a constant value of 1 according to the function

$$\alpha = \max\left(\frac{x - x_s}{x_m - x_s}, \frac{y - y_s}{y_m - y_s}\right). \quad (42)$$

In this case,  $x_s = 15, x_m = 16, y_s = 3, y_m = 4$ . In the range  $x \in [16, 17]$  and  $y \in [4, 5]$   $\alpha$  is set to unity.

Finally, to emphasize hybrid AV - FVSE scheme's ability to stabilize the solution without excessive dissipation we present three blending models. The first represents a purely FVSE scheme;  $\alpha = 0.1$  in all elements, independent of  $\Psi$  (fig. 5a); this will be referred to as the "Constant Alpha Case." The second represents an overly dissipative hybrid AV - FVSE scheme.  $C_m$  is reduced from 0.5 to 0.1, reducing the threshold at which the FVSE scheme will be called (5b); this will be referred to as the "CM1 Case." The third represents a hybrid AV - FVSE scheme that is primarily reliant on the AV scheme and treats the FVSE as a "parachute" (fig. 5c). Here the AV coefficients are  $(C_\mu, C_\kappa, C_m) = (0.5, 0.5, 0.5)$ . This will be referred to as the "CM5 Case." In all cases  $\sigma = 5$  (26).

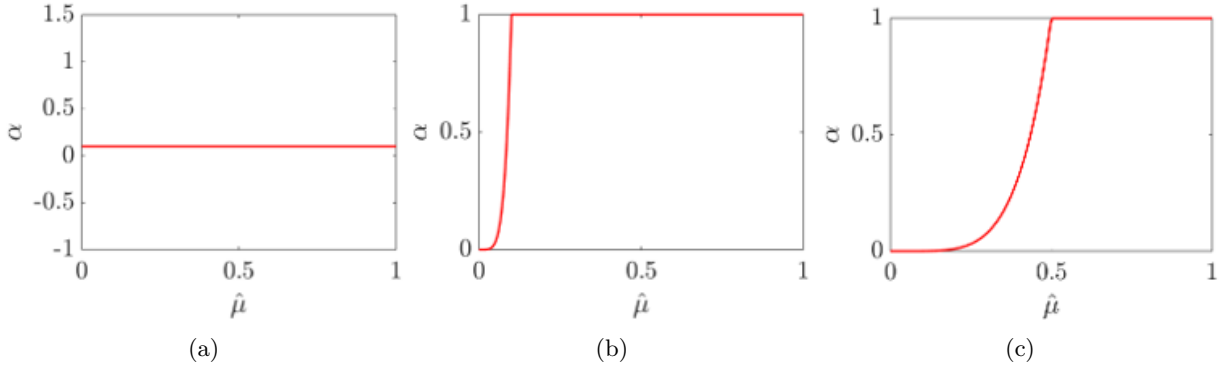


Figure 5: The FVSE blending coefficient,  $\alpha$ , for various shock indicator functions,  $\Psi$ , and AV,  $(C_\mu, C_\kappa, C_m)$ . (a):  $\Psi = 0.1$  (constant  $\tilde{\alpha}$ ),  $(C_\mu, C_\kappa, C_m) = (0.5, 0.5, 0.5)$ . (b):  $\Psi$  is defined by (27),  $(C_\mu, C_\kappa, C_m) = (0.5, 0.5, 0.1)$ . (c):  $\Psi$  is defined by (27),  $(C_\mu, C_\kappa, C_m) = (0.5, 0.5, 0.5)$ .

## 4.2 Under Expanded Mach 2 Jets

In a second test case we investigate an under expanded flow over the aerospike nozzle. The jet flow is Mach 2 at the thruster exit and is accelerated to Mach 5. State variables at the thruster exit and the ambient are equivalent to the perfectly expanded Mach 2 and 5 cases respectively. All values are reported in table 3.



Rather than the three sectioned impinging jet flow initialization (fig. 4) this case is initialized only near the inlet by a Mach 2 jet up to a distance,  $L_u < L_s$ , from the inlet over the ramp (fig. 6). With this initial condition a flow evolution of the expanding jet is computed by the Navier-Stokes solver. We choose  $L_u = 0.025$ ; this initializes the shock front 2 elements away from the inlet boundary allowing any numerical oscillations to be dissipated before interacting with the boundary conditions. Such interactions may generate spurious pressure waves or numerical instabilities as the flux at the inlet oscillates in an attempt to impose a uniform boundary condition.

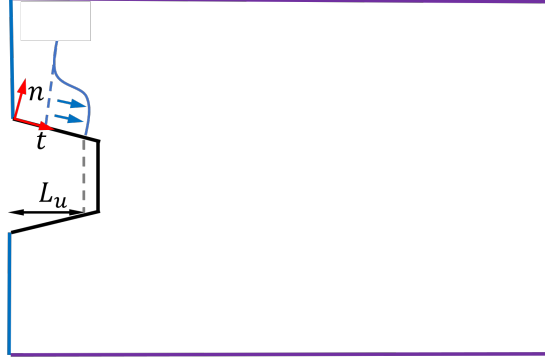


Figure 6: The computational domain of the under expanded Mach 2 jets case. Inlet, outlet, and slip wall conditions are demarcated by blue, purple, and black lines respectively. The velocity field is initialized with a Mach 2 jet flowing a distance  $L_u$  over the aerospoke.

	$\rho$	$U$	$T$	$p$	$M$
<i>o</i>	4.35	0	0.45	1.40	0
<i>e</i>	1	1	0.25	0.18	2
<i>a</i>	0.05	0	0.08	0.0026	0
<i>f</i>	1.24 [kg/m <sup>3</sup> ]	676 [m/s]	1137 [K]	576,288 [Pa]	1

Table 3: Non-dimensional values used in the under expanded Mach 2 jets case. Points "o", "e", and "a" are found in the combustion chamber, at the thruster exit, and in the ambient respectively (fig. 2). "f" indicates the reference values.

The AV coefficients are  $(C_\mu, C_\kappa, C_m) = (0.5, 0.5, 0.5)$  and the implementation of the damping layer is identical to the perfectly expanded cases. The developing expansion fans at the sharp spike tips corners prove particularly difficult to stabilize and the  $\alpha = 1$  radius is increased from  $R = 0.0125$  to  $R = 0.2$  for the first two convective time units,  $\tau$ , of the simulation. Afterwards, the  $\alpha = 1$  radius is returned to  $R = 0.0125$ . Attempts made to return to  $R = 0.0125$  at  $t = [0.5, 1, 1.5, 1.75]$  failed.

### 4.3 Under Expanded Mach 2 Jets With Thrusters

The final case we consider is again an under expanded, non-combusting Mach 2 flow for a computational model that includes a converging - diverging thruster module section upstream of the inlet. This model is representative of a modular aerospoke nozzle propulsion system (fig. 1). The flow is initialized at  $M = 0.3$  in the subsonic section of the thruster module. It accelerates to Mach 2 through the thruster and to Mach 5 over the aerospoke. Stagnation and ambient variables match those of the under expanded Mach 2 flow without thruster modules. Inlet values are computed from the stagnation variables. Mach 0.3 is chosen as the inlet Mach number because a compressible flow solver is used and  $M = 0.3$  is the canonical demarcation of compressible flow.

The wall contour of the supersonic section of the thruster module is designed using an in-house method of characteristics (MoC) solver. This MoC solver has been validated in previous supersonic nozzle investigations [48]. A thruster exit Mach number of  $M_e = 2$  is chosen to maintain congruity with the previous

cases. To compute the minimum length nozzle contour a Prandtl-Meyer expansion fan accelerating the flow from Mach 1 to  $M_e$  is initialized at the thruster throat. The contour is then computed such that it is tangent to the flow angle where characteristics impinge along the wall. For more detailed description of this process we refer to Chapter 11.7 of the textbook by Anderson [3].

The wall contour of the subsonic section is computed by fitting a  $\cos(x)$  function to the constraints:

$$\begin{aligned} g(x_t) &= f(x_t) \\ g(x_i) &= y_i \\ g'(x_t) &= 0 \\ g'(x_i) &= 0, \end{aligned} \tag{43}$$

where  $g(x)$  and  $f(x)$  represent the subsonic and supersonic wall contours respectively. These constraints ensure the subsonic contour will join the supersonic contour continuously, a Prandtl-Meyer fan will develop at the throat, and the the inflow to the subsonic section will be uniform.  $y_i$  is defined as  $A_i/2$  where  $A_i$  is the area required to achieve  $M = 0.3$ , assuming  $A_t = 1$ . The resulting contour is:

$$g(x) = \frac{y_i - y_t}{2} (1 + \cos(\pi \frac{x - x_i}{x_t - x_i})) + y_t \tag{44}$$

A straight section of length 0.25 is then prepended to the subsonic contour model a combustion chamber.

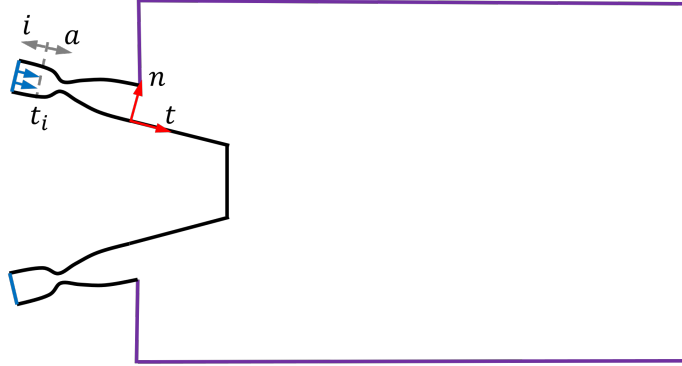


Figure 7: The computational domain of the under expanded Mach 2 jets with thruster modules case. Inlet, outlet, and slip wall conditions are demarcated by blue, purple, and green lines respectively. At locations  $t < t_i$  the flow is initialized with uniform Mach 0.3 flow and for  $t > t_i$  flow is initialized as stagnant air at ambient conditions (Tab. 4).

The case is initialized in the  $n - t$  frame such that

$$\tilde{Q} = \begin{cases} \tilde{Q}_i & t \leq t_i \\ \tilde{Q}_a & t > t_i \end{cases},$$

where "i" and "a" denote the inlet and ambient values respectively (tab. 4).  $t_i = -1.4$  is chosen; this is the midpoint of the prepended "combustion chamber" upstream of the subsonic nozzle contour. The ambient condition is imposed at the outlets and the uniform Mach 0.3 condition is imposed at the inlet. The thruster and aerospike nozzle walls are adiabatic, slip walls.

The AV / FVSE implementation is similar to the under expanded Mach 2 jets case without thruster modules.  $(C_\mu, C_\kappa, C_m) = (0.5, 0.5, 0.5)$  and the implementation of the damping layer is identical to the previous cases expanded cases. The only difference is the  $\alpha = 1$  radius is increased from  $R = 0.0125$  to  $R = 0.2$  for the first three convective time units rather than the first two because initializing the flow in the thruster module delays the formation of the spike tip expansion fans. Within the thruster modules  $\alpha = 1$ ; Once developed, flow through a minimum length converging - diverging nozzle with slip walls is and smooth and isentropic, thus the high fidelity DGSEM scheme is not necessary. No special treatment of the upper and lower thruster tips, or cowl tips, are required despite the presence Prandtl-Meyer expansion fans.

	$\rho$	$U$	$T$	$p$	$M$
<i>o</i>	4.35	0	0.45	1.40	0
<i>a</i>	0.05	0	0.08	0.0026	0
<i>f</i>	1.24 [kg/m <sup>3</sup> ]	676 [m/s]	1137 [K]	576,288 [Pa]	1

Table 4: The non-dimensional values used in the under expanded Mach 2 jets with thruster modules case set up. "o", denotes the stagnation values, "i" denotes the inlet values, and "a" denotes ambient values.

## 5 Results

Before discussing the efficacy of the hybrid AV - FVSE solver for simulation of supersonic and hypersonic flow over an aerospike nozzle, we first conduct a grid study. The effect of dissipation of the FVSE dominated and AV dominated shock capturing schemes are then assessed and the robustness of the AV - FVSE scheme is demonstrated on perfectly expanded and underexpanded hypersonic flow with and without a nozzle.

### 5.1 Error Validation and Grid Study

To verify the spectral accuracy of this solver in the absence of the hybrid shock capturing scheme we compute the  $Re = 100, M = 0.1$  flow over a square cylinder investigated by Klose et al. [34]. The solution is computed using Legendre - Gauss - Lobatto quadrature, the split - form approximation, and a  $P = 3$  polynomial. In a log-log plot of the error in reattachment point location downstream of the cylinder,  $x_u$ , theoretical convergence [35] at the rate  $P + 1 = 4$  is recovered (fig. 8b). The computed Strouhal number of the lift coefficient,  $C_L$ , is 0.145; this is in excellent agreement with the findings of Klose et al. [34].

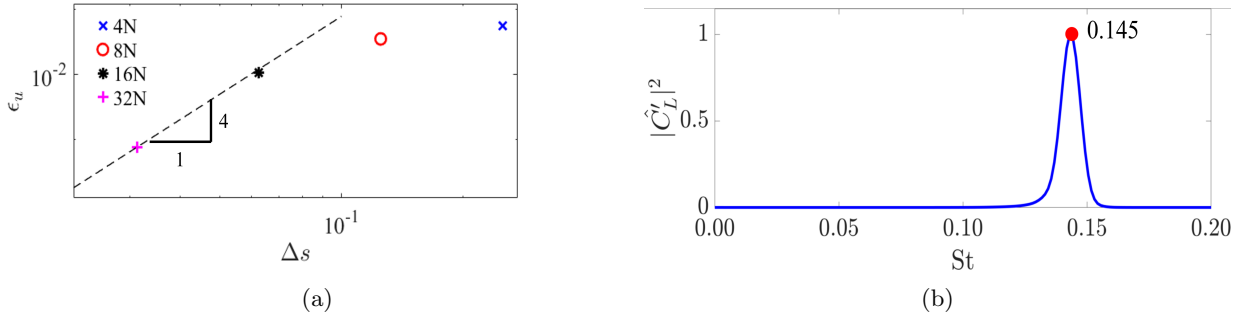


Figure 8: (a) The error in reattachment location,  $x_u$ , demonstrating formal  $P + 1$  convergence and (b) the power density spectra of the wake generated by  $Re = 100, M = 0.1$  flow over a cylinder.

To establish grid independence the perfectly expanded Mach 2 flow case is computed on five meshes that are consistently refined by a factor two in each direction:  $\frac{1}{\Delta s} = 8, 16, 32, 64, 128$  (fig. 9a, 9b). Element aspect ratios are  $\Delta x/\Delta y = 1$  at the spike tip and the aspect ratio is increased in the  $x$  and  $y$  directions by a factor of 1.005 and 1.01 respectively. A maximum aspect ratio of 1.5 is imposed. Greater aspect ratios regularly produce numerical instabilities because shocks propagate through the cells in both the  $x$  and  $y$  directions thus sufficient resolution is required in both directions. The solution is approximated by a  $P = 3$  polynomial, which is often used for complex geometry and high-speed flow computations [10, 27].

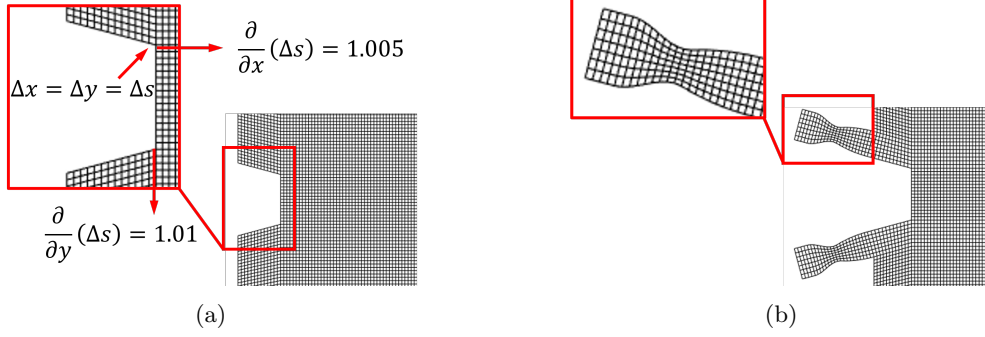


Figure 9: An example of a grid over domains (a) without and (b) with thruster modules. In the wake the grid is uniformly coarsened in the  $x$  and  $y$  directions by factors of 1.005 and 1.01 respectively. A uniform grid spacing,  $\Delta s$ , is applied at the thruster exit plane and along the central thruster axis to create the elements within the thruster module.

The rearward reattachment point,  $x_u$ , at which the supersonic jets merge along the centerline and the integrated pressure along the spike base are chosen as the convergence metrics. The mean flow reattachment point varies in time as the wake oscillates in the open configuration, thus a converged reattachment location indicates wake fluctuations are adequately captured. The integrated base pressure is of interest from the engineering perspective as it directly affects the net thrust generated by the aerospike nozzle and is commonly used in grid convergence studies of the steady state flow field [23, 40, 41].

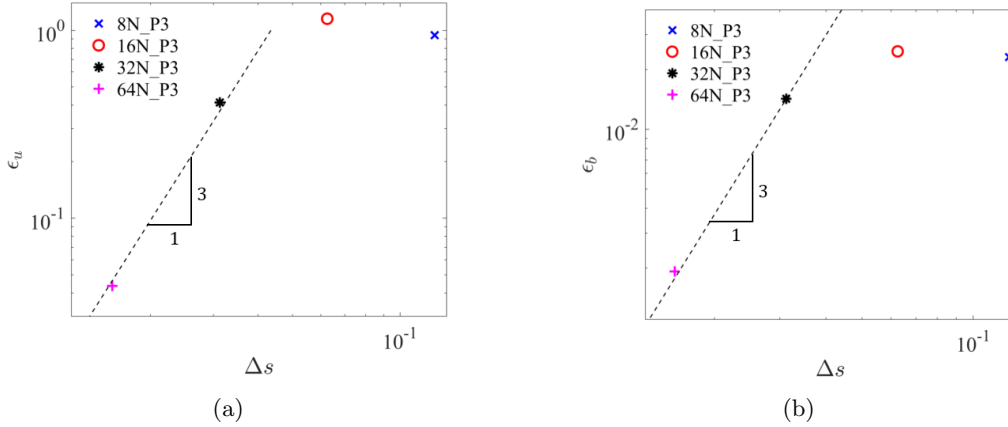


Figure 10: The error of (a) the mean jet reattachment location,  $\epsilon_u$ , and (b) the mean non-dimensional base pressure,  $\epsilon_b$ , as a function of grid spacing. The black dotted lines are reference slope 3 lines.

In log-log plots of the error of the mean jet reattachment location,  $x_u$ , and the integrated spike base pressure,  $\bar{p}_b$ , as a function of grid spacing a slope of 3.24 and 2.88 is recovered (fig. 10a, 10b). The logarithmic error decay demonstrates the solution is in the asymptotic range, although the  $P+1$  convergence slope expected of the DG scheme [35] is not observed. This degradation of global accuracy order is attributed to a cumulation of local diffusive error introduced by the low order shock capturing scheme. The approximate  $P$  scaling is, however, greater than the first order convergence reported by Peck et al. [44] when investigating order of accuracy of an FVSE scheme in which the shock indicator,  $\Psi$ , is the modified Ducros switch (21) rather than the artificial viscosity ratio (27).

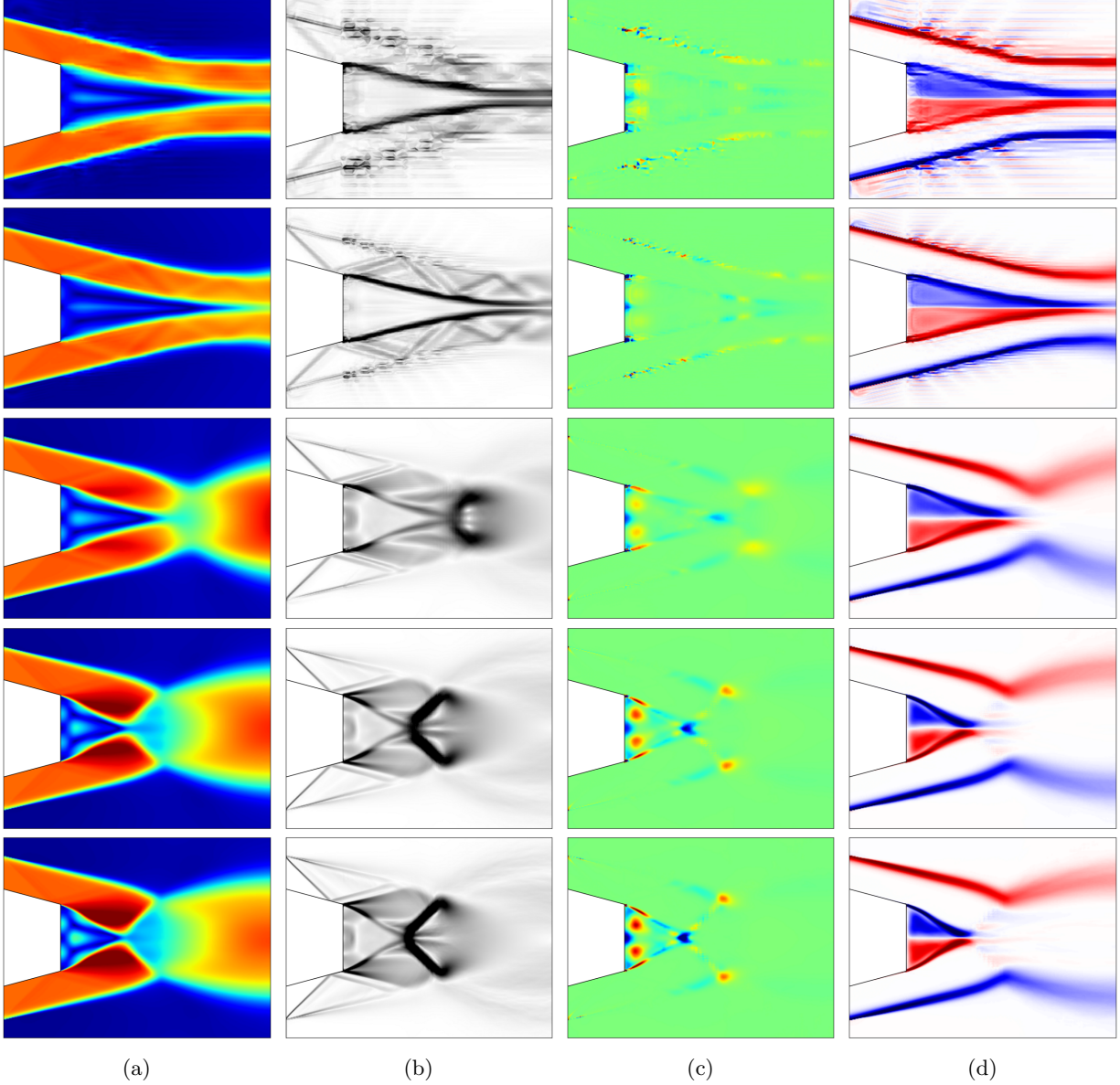


Figure 11: Contours of (a) Mach number, (b) Numerical schlieren, (c) Q-criterion, (d) and vorticity of the time averaged flow field computed over each grid. From top to bottom= the grids are:  $8N$ ,  $16N$ ,  $32N$ ,  $64N$ ,  $128N$ .

All computations in the following sections are conducted on the  $64N$  grid. The geometry without a thruster contains 333,016 elements, resulting in 5,328,256 degrees of freedom for a  $P = 3$  approximation in each element. The geometry with a thruster contains 337,966 elements, resulting in 5,407,456 degrees of freedom for a  $P = 3$  approximation in each element.

## 5.2 Perfectly Expanded Mach 2 Jets

To examine the influence of the hybrid blending functions on the flow, we compute a Mach 2 flow over the aerospike nozzle using the three formulations described in Section 3.4 In the first formulation, the Constant Alpha case,  $\alpha$  is explicitly set to 0.1. In the second formulation, the CM1 case,  $\alpha$  is computed according to (26) and (25) and the AV coefficient  $C_m$  is 0.1. In the third formulation, the CM5 case,  $\alpha$  is again computed

according to (26) and (25) however the AV coefficient  $C_m$  is 0.5. Increasing  $C_m$  from 0.1 to 0.5 shifts the  $\alpha - \hat{\mu}$  curve such that the FVSE scheme is blended into fewer elements (fig. 5b, 5c). The CM5 case may be viewed as a "parachute scheme", where the artificial viscosity serves as the primary stabilization method and the FVSE scheme is deployed only in the presence of extreme gradients.

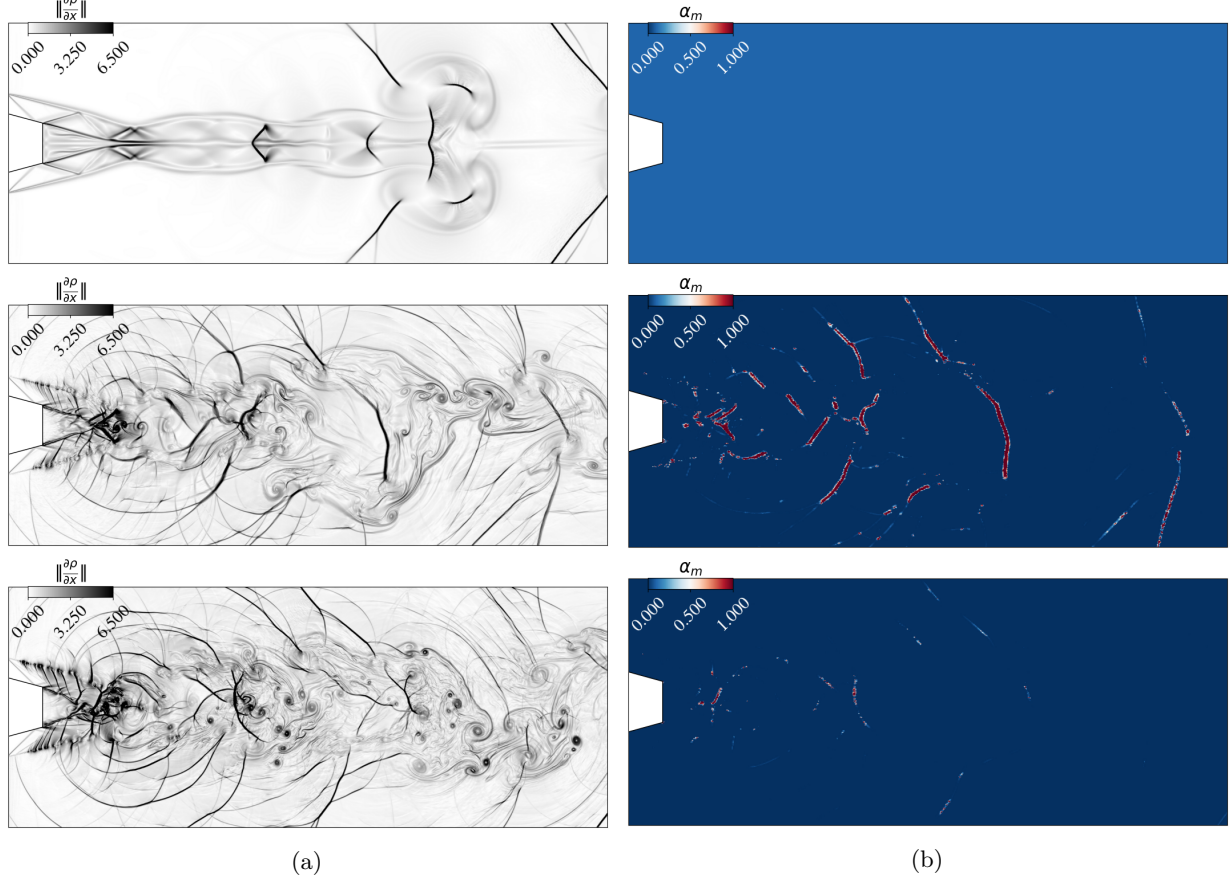


Figure 12: Contours of (a) numerical schlieren images and (b) the FVSE blending coefficient,  $\alpha$ , at time  $t = 25\tau$ . From top to bottom the cases shown are Constant Alpha, CM1, and CM5.

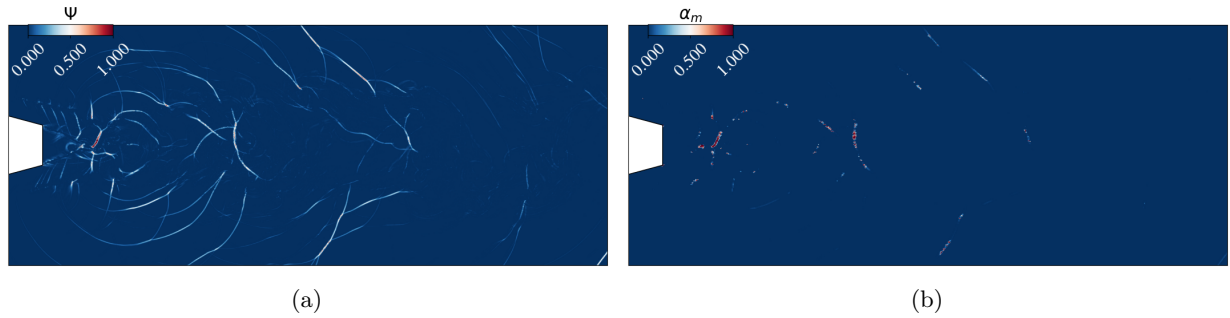


Figure 13: Contours of (a) the shock indicator,  $\Psi$ , (27) and (b) the FVSE blending coefficient,  $\alpha$ , at time  $t = 25\tau$ .  $\alpha$  is computed according to (25), (26), (27) and the AV coefficients are  $(C_\mu, C_\kappa, C_m) = (0.5, 0.5, 0.5)$ .

In the Constant Alpha case no discernible shear instabilities along the outer shear layer of the jet and dividing streamline bounding the recirculation region are present in the schlieren images (fig. 12a). In fact,



the schlieren images are qualitatively similar to RANS investigations of comparable flows [61, 41, 56], where the effect of turbulence stresses is modeled by the standard gradient models that scale with a turbulence viscosity. This is a clear indication that the highly dissipative FVSE scheme suppresses major instabilities.

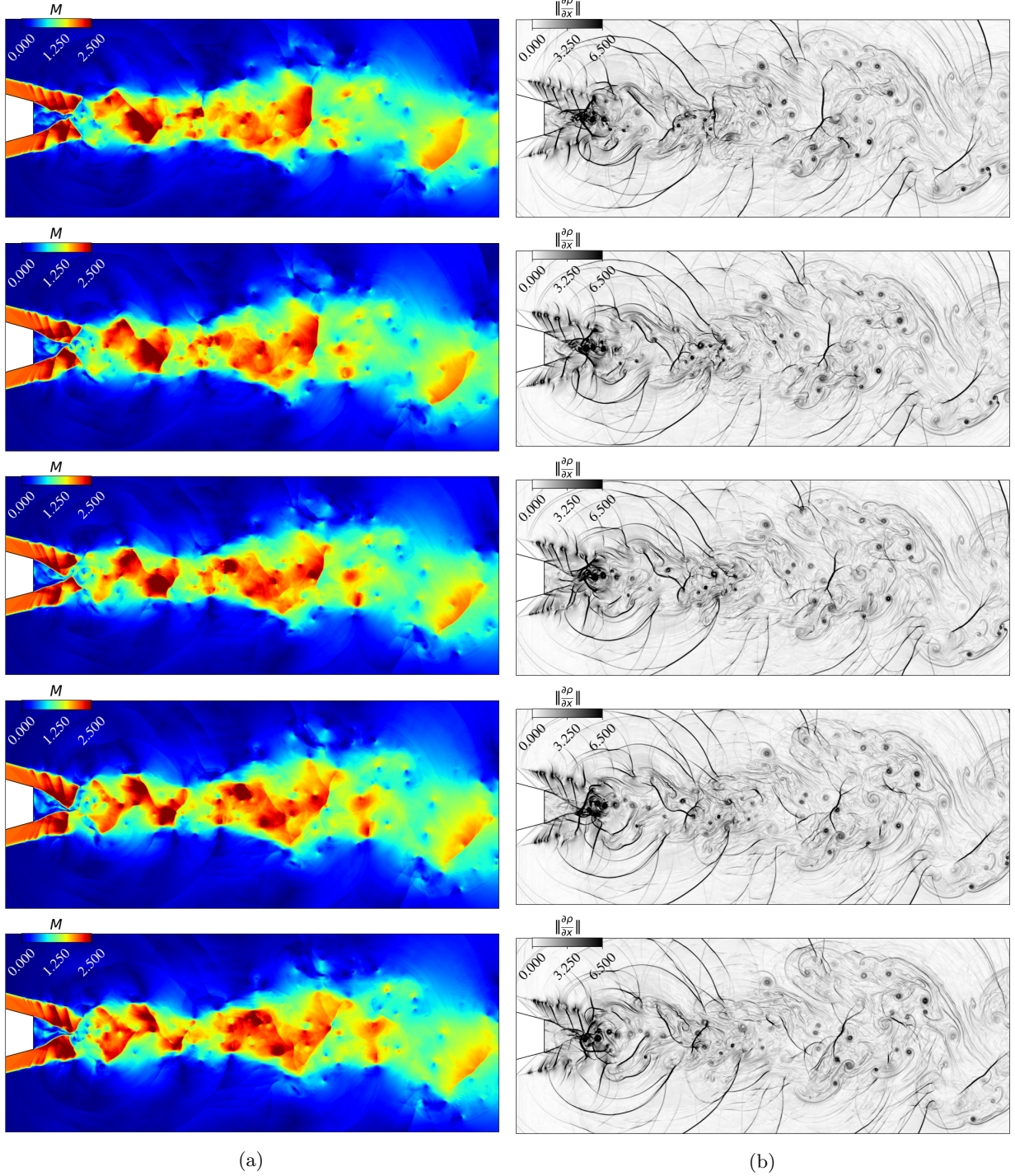


Figure 14: Snapshots of (a) Mach contours and (b) numerical schlieren images of the perfectly expanded Mach 2 flow. From top to bottom the visualized times are:  $t = 100\tau, 100.5\tau, 101\tau, 101.5\tau, 102\tau$ .

In the schlieren images of the CM1 and CM5 cases shear instabilities are observed. Pressure waves form as the outer shear layer is perturbed and deflects the supersonic jet flow inwards towards the spike. These waves impinge on the dividing streamline between the supersonic jet and the recirculation region (fig. 12). Vortices form along the wake centerline and shock - vortex interactions occur in the wake downstream of the jet reattachment point. The excessive numerical diffusion of the Constant Alpha case dissipate these flow features and the unsteady behavior and associated dynamics are not captured.

By steepening the blending function AV serves as the primary shock capturing method, while FVSE takes on the role of a "parachute" to smooth extreme gradients that cannot be regularized by AV without incurring excessively small time steps. This is done by increasing  $C_m$ , thus increasing the  $\mu_h$  required to achieve a  $\Psi = 1$  shock indicator value (27). The number of elements in which  $\alpha \rightarrow 1$  in the non-steepened CM1 case is greater than in the steepened CM5 case (fig. 12b). As a result small vortices and pressure waves in the wake that were previously obfuscated are captured. The "parachute" behavior of the FVSE after steepening the blending function can be seen when comparing the AV based shock indicator,  $\Psi$  (27), and the FVSE blending coefficient,  $\alpha$  (26), in Figure 13.  $\alpha$  is non-zero in only a fraction of the elements in which the shock indicator is non-zero, demonstrating that the AV is functioning as the primary shock capturing method. In all proceeding results the CM5 formulation is used:  $(C_\mu, C_\kappa, C_m) = (0.5, 0.5, 0.5)$  and  $\sigma = 5$  (26). This formulation reduces the numerical dissipation introduced by the highly diffusive FVSE scheme, enabling the unsteady dynamics of the supersonic aerospike nozzle wake to be captured without excessive numerical dissipation.

The oscillations in the wake observed in instantaneous Mach and numerical schlieren contours (fig. 14) are driven by a feedback loop between the wake and the supersonic jets; this is illustrated schematically in Figure 15. Shear instabilities form along the outer shear layer, generating pressure waves in the ambient and shocks within the jet that are advected downstream along the shear layer. The interior shock waves impinge upon the dividing streamline, inducing oscillations in the streamline that are transmitted to the reattachment shocks. As the shear instabilities along the outer shear layer interact with these oscillating reattachment shocks vortices and packets of supersonic fluid are ejected, and the exterior pressure waves propagate upstream through the ambient. The upstream propagating pressure waves perturb the outer shear layer, further driving the formation of the exterior pressure waves and interior shocks and completing the feedback loop between the wake, subsonic recirculation region, and supersonic jets.

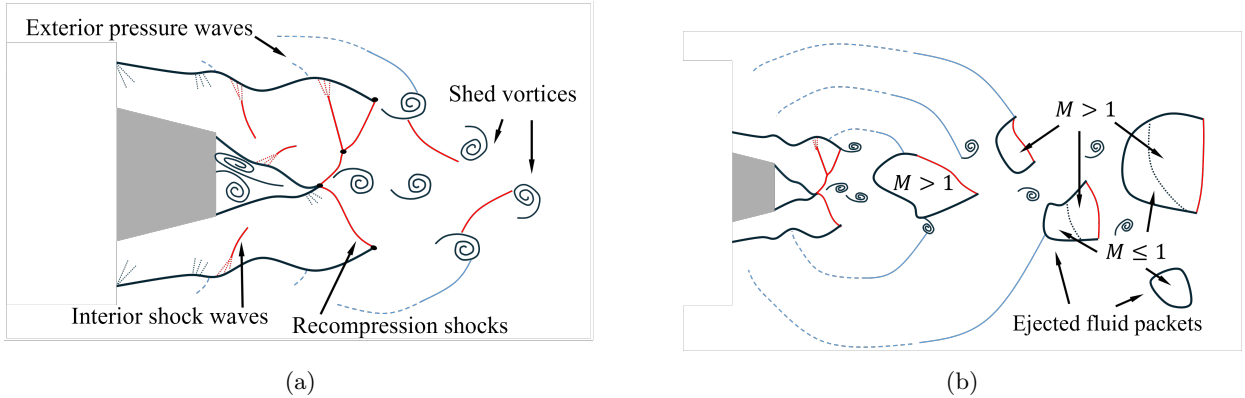


Figure 15: (a) Zoomed in and (b) zoomed out schematic of the perfectly expanded Mach 2 jet flow wake. Vortices are intermittently shed along the wake centerline and the outer shear layers. Perturbations along the outer shear layer generate exterior pressure waves and interior shock waves. The pressure waves attach to ejected fluid packets, propagate upstream, and perturb the outer shear layer to form a feedback loop.

The wake oscillations generate an unsteady pressure force on the aerospike nozzle. The power spectral density of the time-dependent, non-dimensionalized pressure forces in the  $x$  and  $y$  direction,  $C_D$



and  $C_L$ , are plotted vs Strouhal number in Figures 16b and 16a.  $St$  is defined as:

$$St = \frac{f \cdot L_f}{U_f}. \quad (45)$$

$L_f$  is computed using the reference Reynolds number,  $U_e$ ,  $\rho_e$ ,  $T_e$ . Peaks are observed in both the  $C'_L$  and  $C'_D$  spectra in the ranges  $St = 0.06 - 0.07, 0.10 - 0.11$ , and  $0.28$ . In Figure 14 the reattachment point completes a single oscillation in approximately two convective time units, or at a non-dimensional frequency of  $St \approx 0.25$ . This suggests the  $St = 0.28$  frequency in the  $y$  pressure signal is driven by the flapping jets, while the  $St = 0.07$  and  $0.10$  correspond to fluctuations with a period of 10 – 14 convective time units.

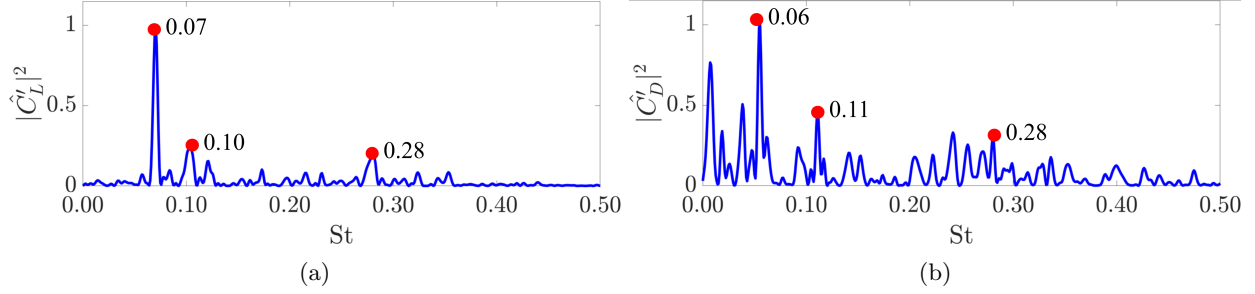


Figure 16: Power spectral density of the unsteady pressure signal in the (a)  $y$  and (b)  $x$  direction in the perfectly expanded Mach 2 case. The signal is sampled at every time step from  $t = 100\tau - 500\tau$ .

### 5.3 Under Expanded Mach 2 Jets

Mach and numerical schlieren contours of the under expanded case without thrusters are visualized in Figure 18. For completeness and for the interested reader, vorticity, and  $Q$  criterion contours are available in Figure 23 in Appendix A. To maintain numerical stability we explicitly assign an  $\alpha = 1$  region about the spike tip corners from  $R = 0.0125$  to  $R = 0.2$  for times  $t \leq 2\tau$  according to (41). This is necessary because the Prandtl-Meyer fan that develops as the jet flow expands over the sharp spike tip is isentropic; thus the entropy generation is negligible and no artificial viscosity is introduced by the AV scheme to smooth the pressure gradient and prevent undershoots in the solution. For times  $t > 2\tau$  the  $\alpha = 1$  region is reduced back to  $R = 0.0125$ . No further adjustments are necessary capture the shock fronts, the upstream propagating supersonic pocket in the recirculation region observed at  $t = 2\tau$ , the triple point observed at time  $t = 8.75\tau$ , or reattachment shocks (fig. 18).

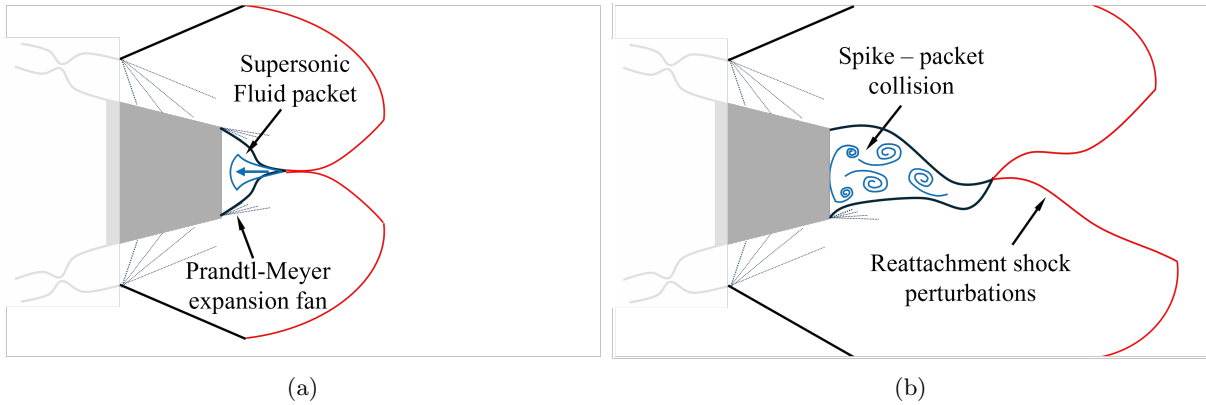


Figure 17: A schematic of the under expanded jet flow without thrusters. (a) An upstream propagating supersonic fluid packet develops in the recirculation region. (b) This packet impinges on the spike base, perturbing the dividing streamline. These perturbations are stabilized by  $t = 100\tau$ . This phenomena occurs over the geometry with and without thruster modules.

Beginning from a quiescent initial state (fig. 6), two convex shock waves are propelled over the spike ramp and collide at the centerline. At time  $t = 2\tau$  an upstream propagating wave is observed in the subsonic recirculation region (fig. 18). By time  $t = 8.75\tau$  the wave collides with the spike base, perturbing the dividing streamline between the recirculation region and the jets and inducing oscillations at the jet reattachment point (fig. 17). Evidence of this is seen in the asymmetry of the recirculation region and the reattachment shocks in the Mach and Schlieren contours (fig. 18). However, by time  $t = 100\tau$  the solution converges to a quasi-steady state.

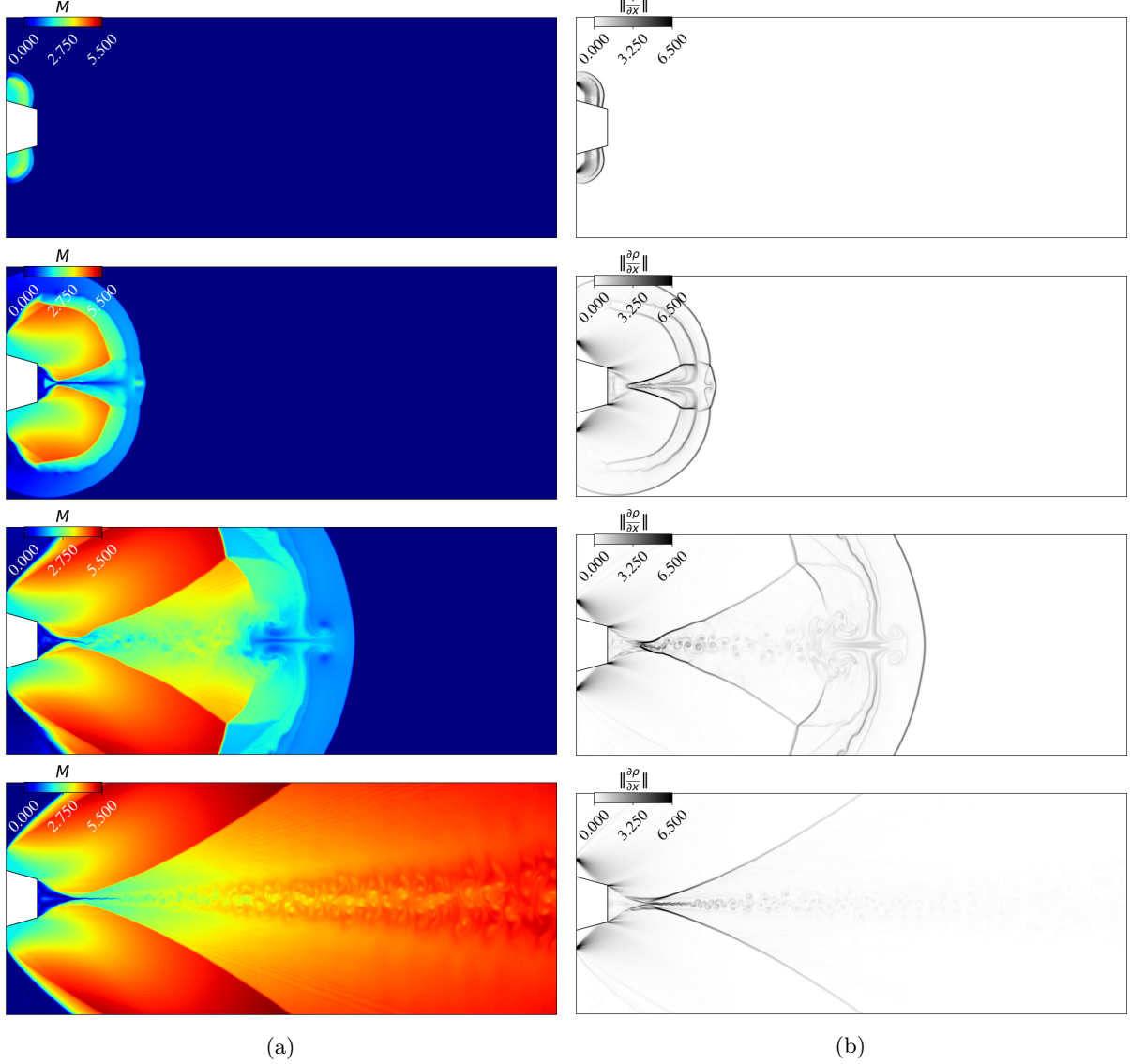


Figure 18: Snapshots of (a) Mach contours and (b) numerical schlieren images at  $t = 0.5\tau, 2\tau, 8.5\tau, 100\tau$  of the under expanded Mach 2 flow without thruster modules.

This quasi-steady state is observed in the under expanded case but not the perfectly expanded case because increasing the Mach number, and thus compressibility, of the jets damps perturbations along the dividing streamlines between the supersonic jets and the recirculation region. This phenomena is well documented for compressible wakes: The linear instability analysis by Chen et al. [11] shows the growth rates of instabilities in the shear layers of a plane wake decrease by as much as 30% between an incompressible

and Mach 3 free stream. Harris and Fasel [26] conduct DNS of a Mach 2.46 wake and observe no instabilities along the shear layers in unperturbed wakes at  $Re \leq 100,000$ . Bashkin et al. [6] reports the stabilizing effect of compressibility in supersonic cylinder wakes with a computational RANS model study in which a the laminar - turbulent wake transition occurs at  $Re = 30,000$  in a Mach 2 flow and  $Re = 300,000$  in a Mach 5 flow. Thus by increasing the Mach number of the flow over the dividing streamline in the aerospike nozzle instabilities along said streamline are stabilized, and oscillations are not transmitted from the dividing streamline to far wake via the reattachment shocks. Additionally, the reattachment shocks do not impinge on the outer shear layer, so the feedback loop driving the flapping motion seen in the perfectly expanded Mach 2 case cannot form.

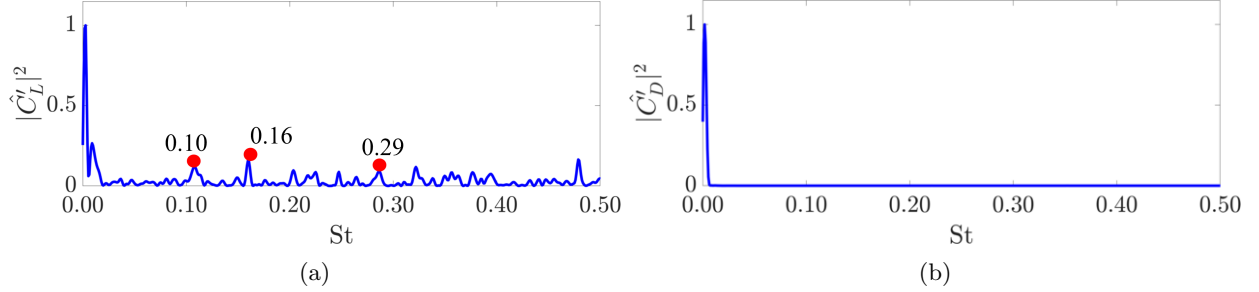


Figure 19: Power spectral density of the (a)  $y$  and (b)  $x$  nozzle forcing in under expanded Mach 2 flow without thruster modules. The signal is sampled at every time step from  $t = 100\tau - 500\tau$ .

Although a seemingly closed, steady wake forms, peaks are present in the power spectrum of the pressure force signal in the  $y$  direction at  $St = 0.1, 0.16$ , and  $0.29$  (fig. 19a). The Strouhal number of  $St = 0.29$  is consistent with experimental investigations by Schmidt and Shepard [50], who detect oscillations in the Mach 3 cylinder wake at the shock reattachment point via high speed schlieren imaging in the range of  $St = 0.3, 0.5$ . By computing the proper orthogonal decomposition of high speed schlieren imaging data of an analogous Mach 3 cylinder wake Awasthi et al. [4] extracted a standing wave pattern within the recirculation region. This wave pattern shares the same frequency of the of the vortex shedding in the wake, suggesting the wake oscillation and resultant vortex shedding is caused by aero-acoustic resonance. They propose that the resonance occurs between the oscillating reattachment point in the wake and the unsteady separation points along the cylinder surface. While it is possible the vortex shedding observed in Figure 18 at time  $t = 100\tau$  is also caused by an aero-acoustic resonance, the resonating structures must be different. The separation points occur at the sharp spike corners and do not shift along the aerospike nozzle surface. A resonance may, however, occur between pressure waves rebounding within the recirculation region and the vortex shedding at the reattachment point. The upstream propagating wave within the recirculation region demonstrates such waves do occur and that they can perturb the dividing streamline and thus reattachment point.

#### 5.4 Under Expanded Mach 5 Jets With Thrusters

In the under expanded Mach 2 case with thruster modules an explicitly assigned  $\alpha = 1$  is created from  $R = 0.0125$  to  $R = 0.2$  for times  $t \leq 3\tau$ ; this is increased by one convective time unit from the reduced domain case to account for the additional time taken by the jets to flow through the thruster modules. For times  $t > 3\tau$  the  $\alpha = 1$  region is reduced to  $R = 0.0125$ . An additional  $\alpha = 1$  region spans the thruster modules. This maintains numerical stability as the flow accelerates to supersonic speeds and a shock front develops.

In the  $t = 0.5\tau$  and  $t = 1.75\tau$  snapshots compression waves form in the subsonic section of the thruster modules as the compressible flow is deflected towards the thruster axes and accelerates. By time  $t = 3.25\tau$  the flow within the thruster modules achieves a steady state. Expansion fans originating at the throat of the thruster module are generated by as the flow is deflected away from the thruster axis by the discontinuous change in curvature at the throat that is characteristic of a minimum length supersonic nozzle.

At time  $t = 9.75\tau$  Kelvin - Helmholtz instabilities develop upstream of the reattachment shock triple points, indicating the solution is not over-damped.

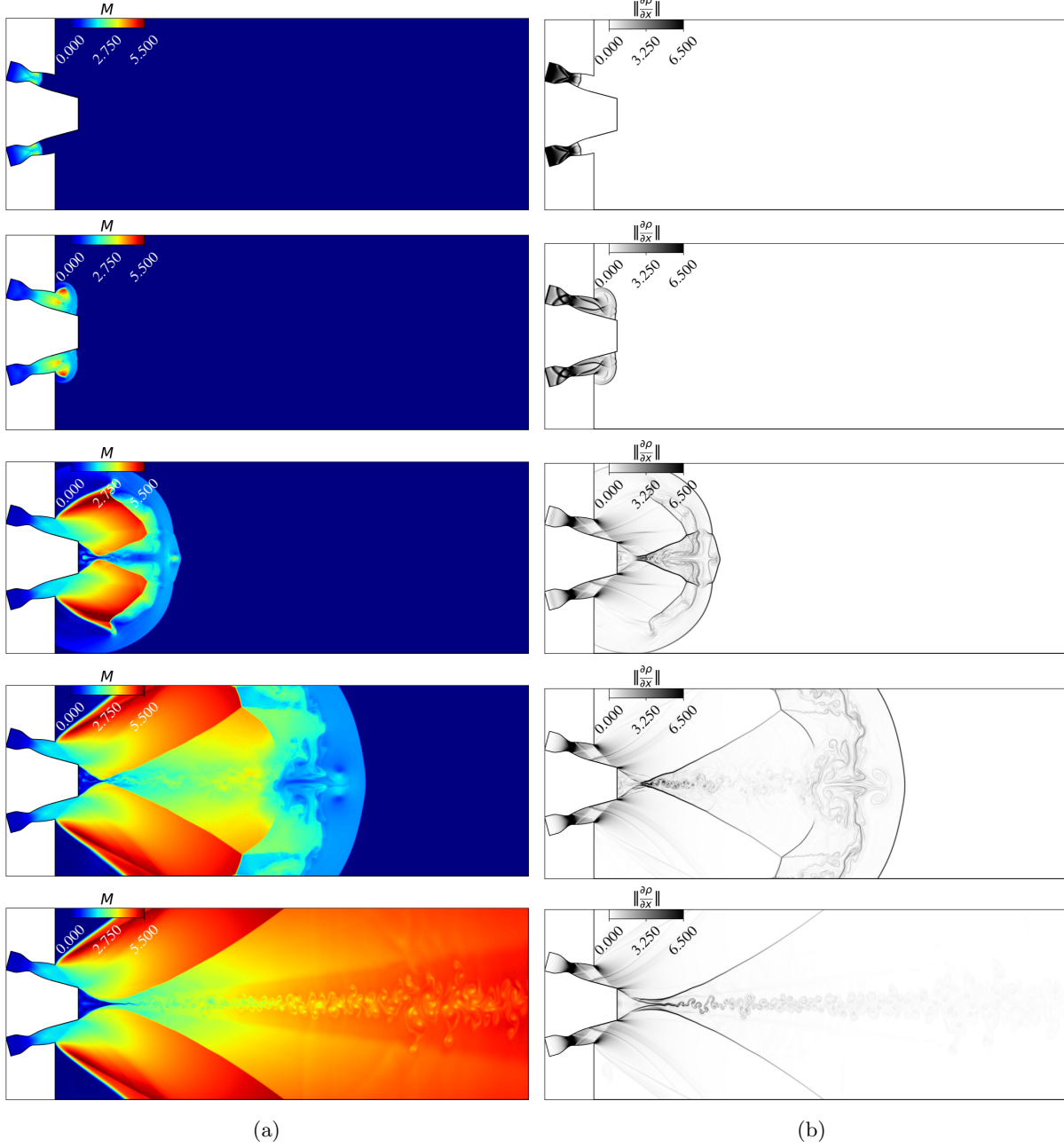


Figure 20: Snapshots of (a) Mach contours and (b) numerical schlieren images at  $t = 0.5\tau, 1.75\tau, 3.25\tau, 9.75\tau, 100\tau$  of the under expanded Mach 2 flow with thruster modules.

As with the thrusterless geometry, the aerospike nozzle wake experiences a transitory state before settling to a quasi-steady state as  $t \rightarrow 100\tau$ . A pocket of supersonic fluid traveling upstream into the recirculation region from the jet reattachment point is observed in the Mach contour at time  $t = 3.25\tau$ . Mach and schlieren contours at  $t = 9.75\tau$  are taken after the fluid pocket collides with the spike base; the unsteady motion in the recirculation region generated by this collision is seen in the asymmetric wave pattern within the recirculation region and the asymmetry of the recompression shocks in the schlieren contour. As time

approaches  $t = 100\tau$  the dividing streamlines and recompression shocks stabilizes.

A flow feature found in the thruster - nozzle assembly case but not in the thrusterless case is the pair of compression waves originating at the upper and lower spike surfaces of the aerospike (fig. 20). These are first observed in the schlieren image at  $t = 3.25\tau$  and remain steadily attached to the joint between the thruster modules and the aerospike nozzle. The waves are caused by a discontinuity in the wall curvature at the joint, which was not explicitly enforced by (43), deflecting the flow towards the thruster axes. In this case the thruster curvature at the joint,  $f'(x = 0)$ , and the nozzle curvature at the joint,  $h'(x = 0)$ , differ by  $O(3 \times 10^{-5})$ . While this compression wave has little qualitative effect on this flow, Pyle et al. [48] demonstrates in a computational RANS model study that wave patterns generated upstream of the aerospike can have dramatic downstream effects, even inducing flow separation and the formation of oblique separation shocks along the spike ramp.

The primary Strouhal numbers in the  $y$  direction pressure signal increase from  $St \leq 0.5$  in the reduced domain (fig. 19a) to  $St \geq 45$  in the non-reduced domain (fig. 21c).  $St = 45$  is the primary frequency with secondary and tertiary frequencies about  $St = 137$  and  $St = 229$ . The dominant frequency in the pressure signal in the  $x$  direction remains at  $St \leq 0.01$ , indicating a near steady axial pressure force. However, a peak at  $St = 45$  is present, suggesting the primary mode of the  $y$  direction forcing influences the  $x$  direction forcing as well. As the computational model of the reduced and non-reduced domains are otherwise identical, this frequency shift must be caused by flow patterns introduced by the thruster modules such as the thruster throat expansion fans or the thruster - nozzle joint perturbation.

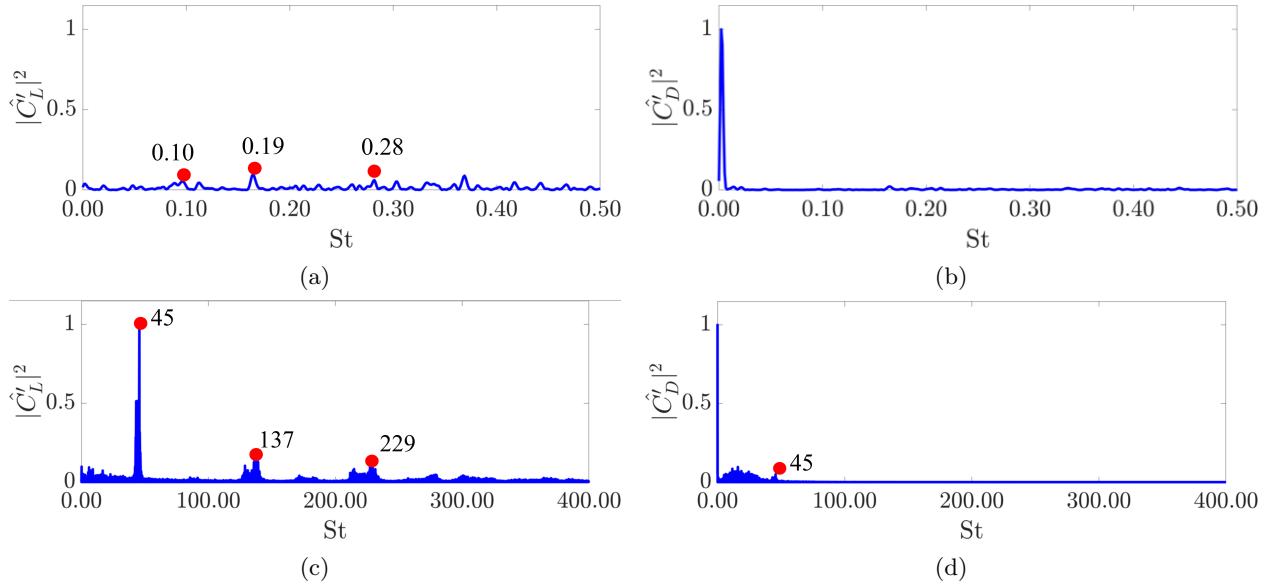


Figure 21: Power spectral density of the (a,c)  $y$  and (b,d)  $x$  nozzle forcing in under expanded Mach 2 flow without thruster modules. Low frequency content ( $St \in [0, 0.5]$ ) is plotted in (a) and (b) and high frequency content ( $St \in [0, 40]$ ) is plotted in (c) and (d). The signal is sampled at every time step from  $t = 100\tau - 500\tau$ .

## 6 Conclusion

In support of developing the next generation of propulsion systems, we present a high fidelity spectral solver well suited for computations of unsteady flow over an aerospike nozzle. To overcome the formidable task of maintaining numerical stability in the supersonic and hypersonic regimes a hybrid artificial viscosity (AV) / finite volume subcell element (FVSE) scheme is developed. A dissipation term is locally introduced to the numerical solution via artificial viscosity where entropy generation is "large" (i.e. at shocks). In elements where the scaled artificial viscosity is above a prescribed threshold a low order finite volume solution is

blended with the high order DGSEM solution. The numerical flux of the low order solution is computed according to the Lax-Friedrichs scheme, ensuring heavy diffusion and monotonicity. We show with judicious choices of the AV coefficients and FVSE blending function this low order solution behaves as a "parachute scheme" and is deployed only in elements with extreme gradients, mitigating loss in accuracy caused by the local blending of the low order solution.

The efficacy of this solver is demonstrated over three progressively complex test cases: perfectly expanded Mach 2 flow over an aerospike nozzle without thruster modules, under expanded Mach 2 flow over an aerospike nozzle without thruster modules, and under expanded Mach 2 flow over though a thruster module - aerospike nozzle assembly. All computations are run for 500 convective time units. Minimal changes to the shock capturing scheme are required to maintain numerical stability between each case, attesting to the general applicability of this solver and shock capturing scheme to supersonic and hypersonic flows over complex geometries. The primary region of instability in each test case is the expansion fans that develop at the spike tip corners; gradients across these isentropic flow features are poorly smoothed by the entropy generation based AV scheme and undershoots in the solution may occur if a monotonic solution is not enforced.

In each test case the power density spectrum of the pressure forcing experienced by the aerospike nozzle is computed and linked to flow features observed in instantaneous snapshots of Mach and schlieren contours. In the perfectly expanded case oscillations in the reattachment shocks generate pressure waves that propagate upstream through the quiescent ambient air. These waves perturb the shear layers of the supersonic jets, feeding the oscillations of the reattachment shocks and forming a feedback loop. In the under expanded cases, both with and without thruster modules, this feedback loop is not observed. As the supersonic jets collide along the centerline a supersonic pocket of fluid propagates upstream through the subsonic recirculation region. This pocket impinges upon the spike base and excites the dividing streamline between the jets and the recirculation region, however these perturbations are damped and a quasi-steady state is achieved. This is attributed to the well documented inverse relationship between Mach number and shear instability growth rates in planar and cylindrical wakes. In the case of the thruster module - aerospike nozzle assembly the primary frequencies in the  $y$  pressure force signal are in the range  $St \in [45, 229]$  rather than the range  $St \in [0, 0.5]$  observed in the perfectly expanded case and under expanded case without thrusters. Additionally, compression waves are observed at the thruster - nozzle joints.



## A Additional Figures

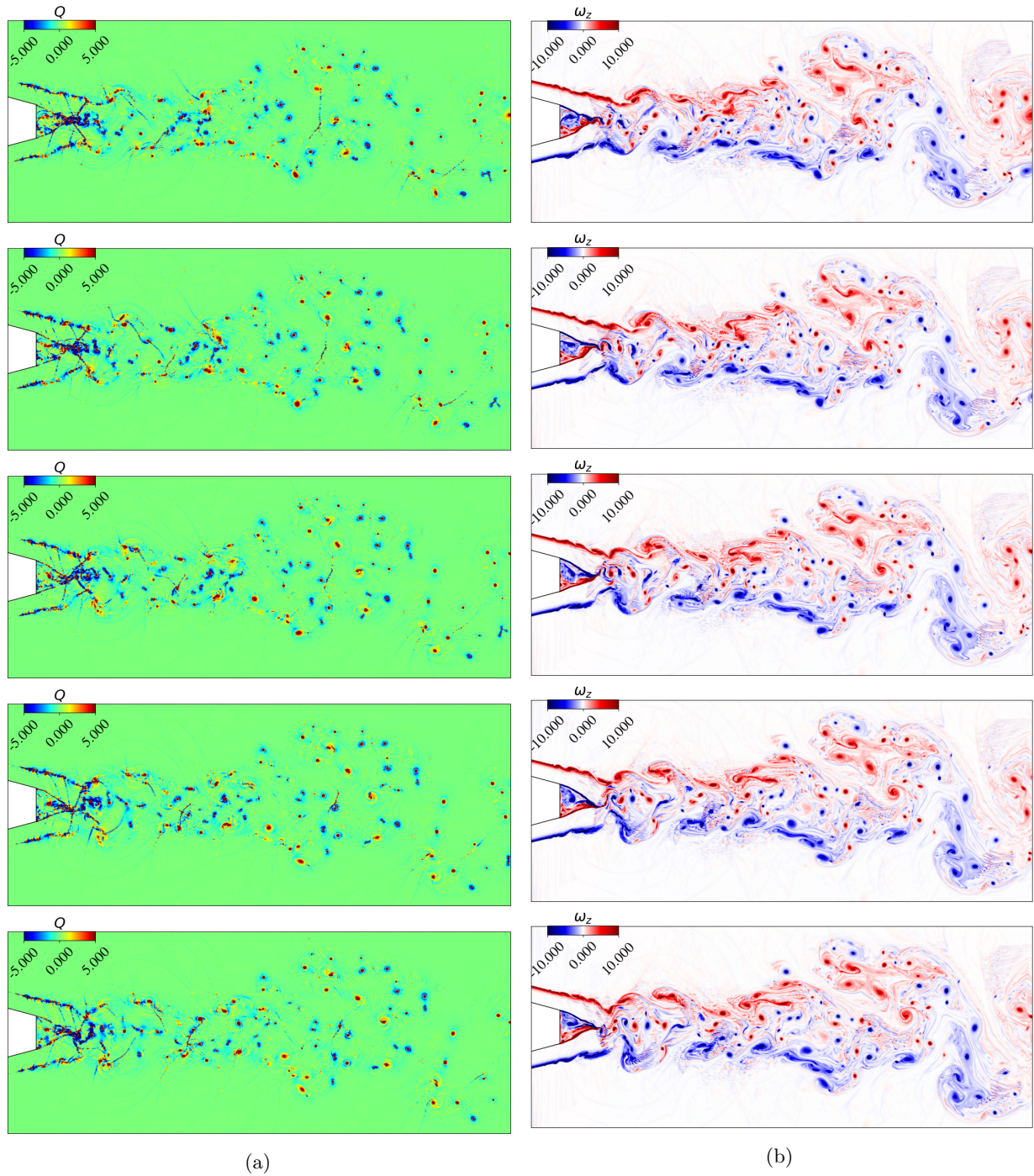


Figure 22: Snapshots of (a) Q Criterion and (b) vorticity of the perfectly expanded Mach 2 flow. From top to bottom the visualized times are:  $t = 100\tau, 100.5\tau, 101\tau, 101.5\tau, 102\tau$ .

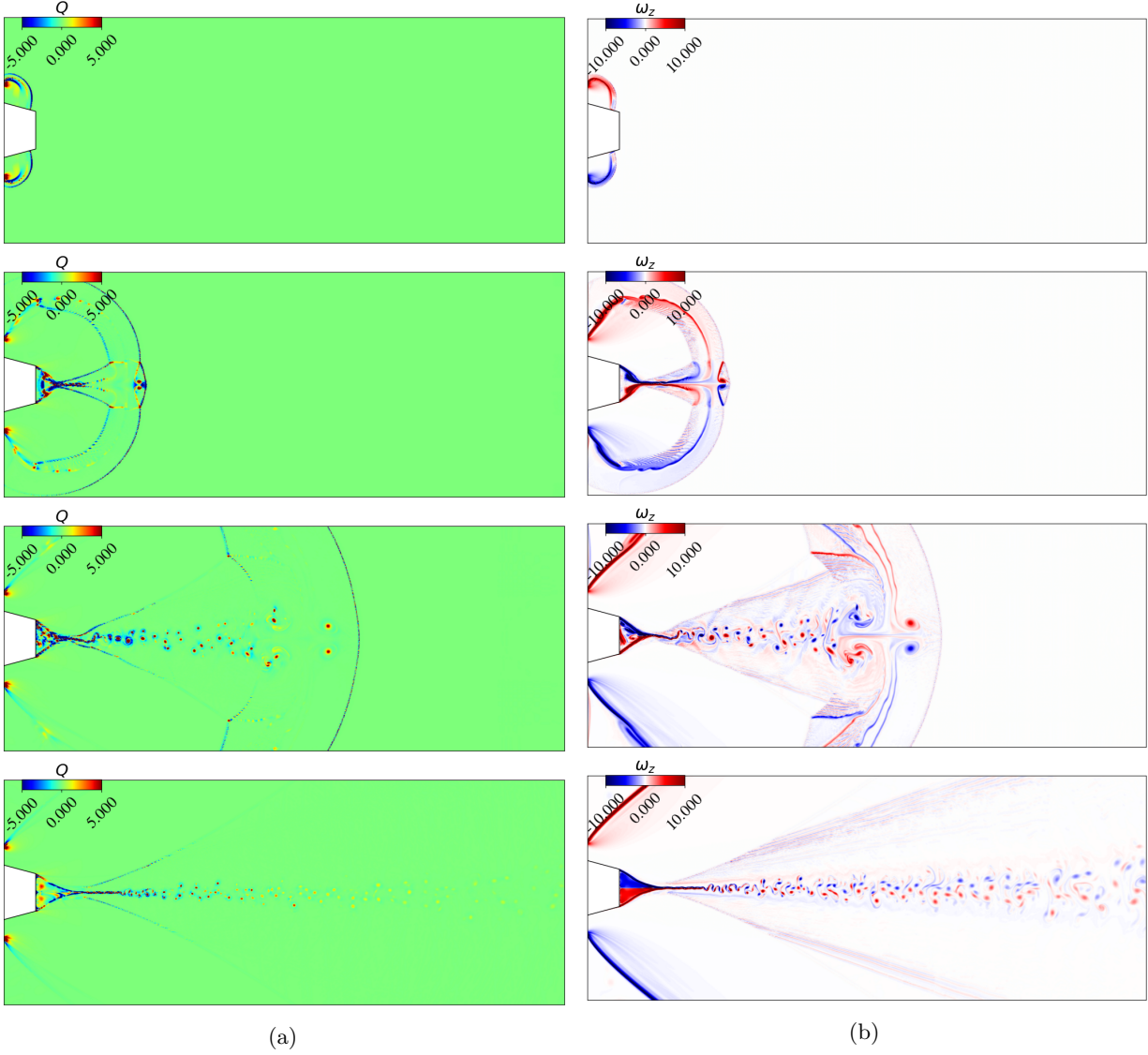


Figure 23: Snapshots of (a) Q Criterion and (b) vorticity at  $t = 0.5\tau, 2\tau, 8.5\tau, 100\tau$  of the under expanded Mach 2 flow without thruster modules.



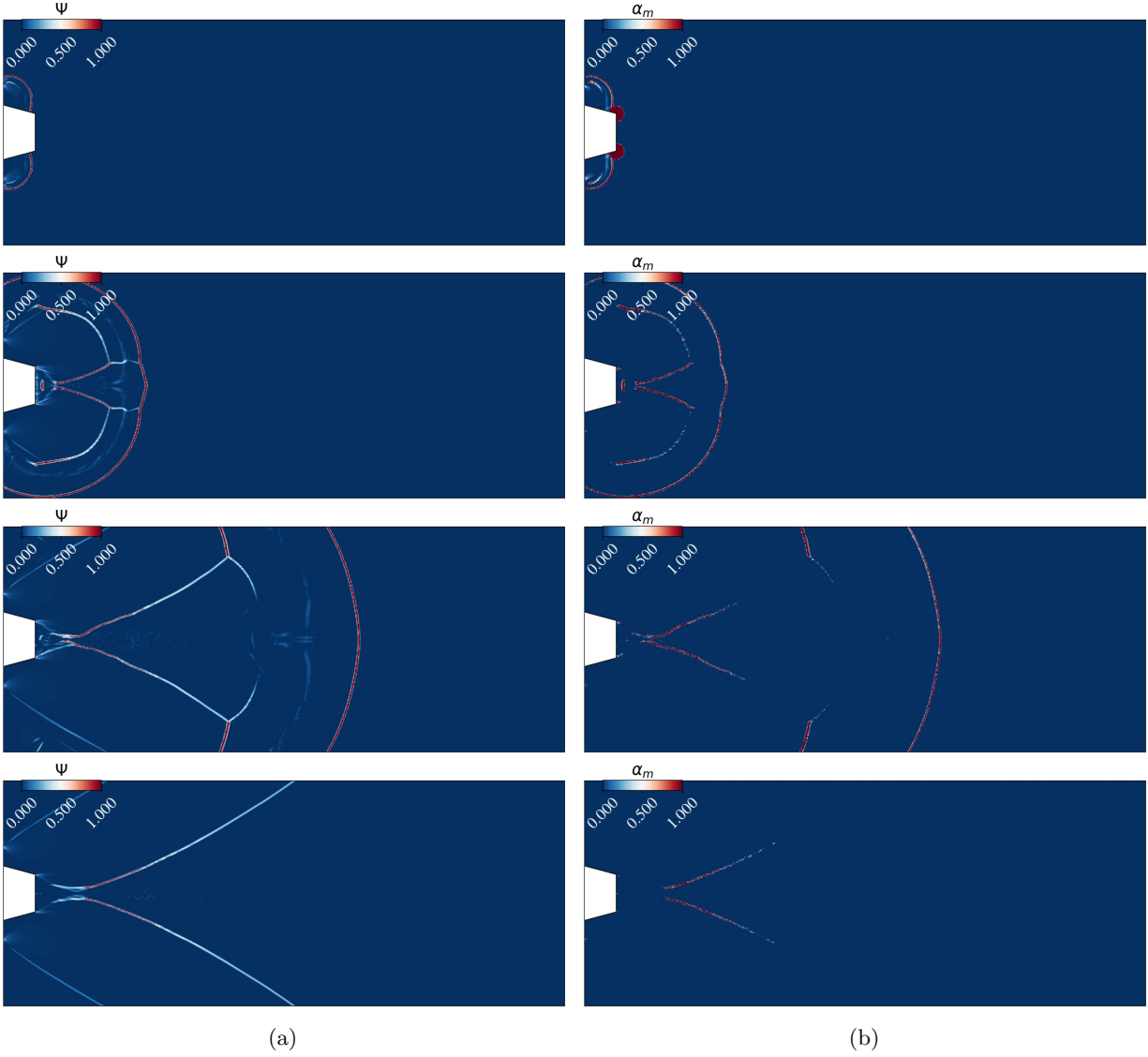


Figure 24: Snapshots of (a) the shock indicator,  $\Psi$ , and (b) the FVSE blending coefficient,  $\alpha$ , at  $t = 0.5\tau, 2\tau, 8.5\tau, 100\tau$  of the under expanded Mach 2 flow without thruster modules.

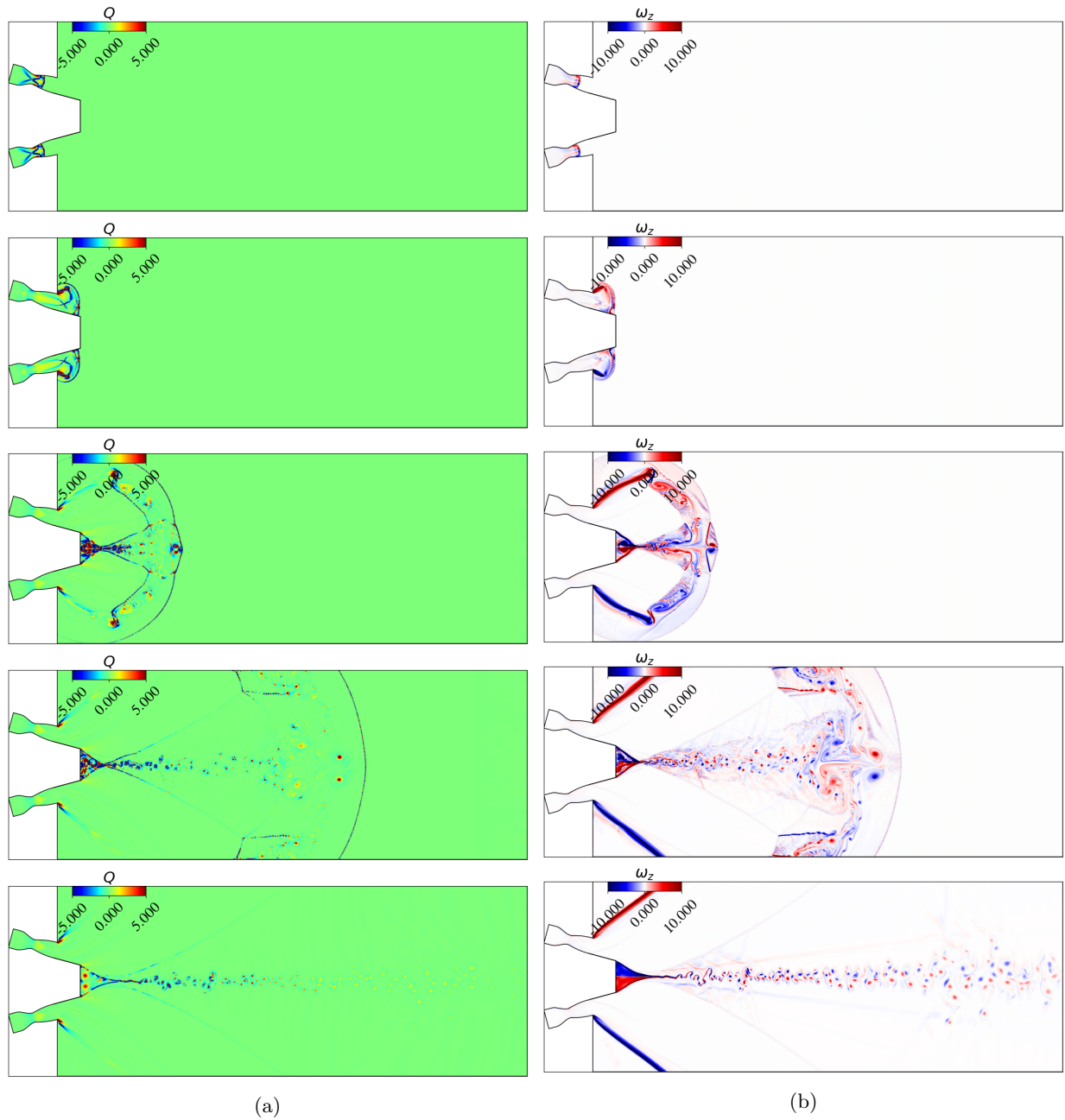


Figure 25: Snapshots of (a) Q criterion and (b) vorticity at  $t = 0.5\tau, 1.75\tau, 3.25\tau, 9.75\tau, 100\tau$  of the under expanded Mach 2 flow with thruster modules.

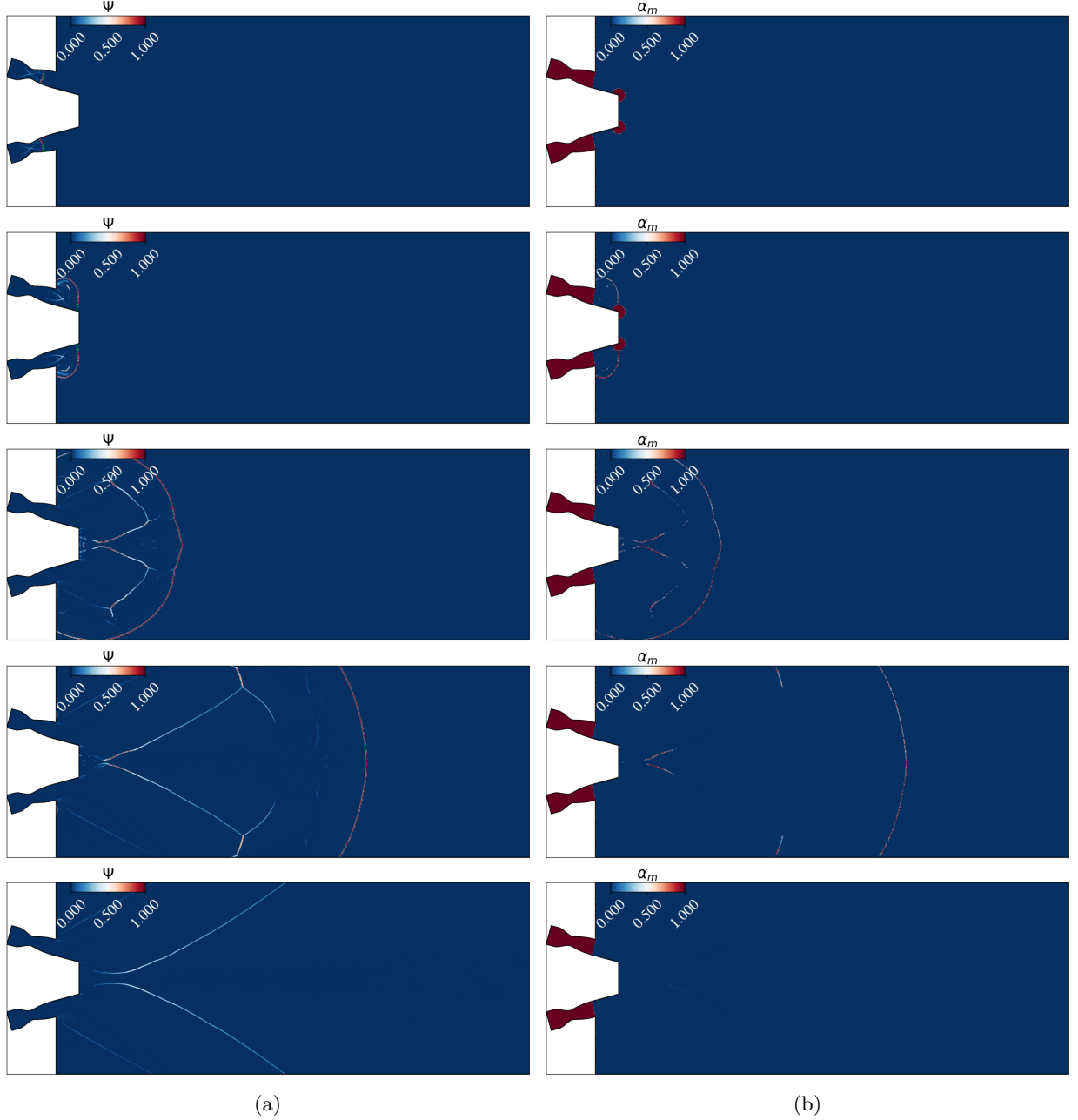


Figure 26: Snapshots of (a) the shock indicator,  $\Psi$ , and (b) FVSE blending coefficient,  $\alpha$ , at  $t = 0.5\tau, 1.75\tau, 3.25\tau, 9.75\tau, 100\tau$  of the under expanded Mach 2 flow with thruster modules.

## Acknowledgments

This work was supported by the Department of Defense Air Force Research Laboratory and under the grant FA930025C6002. Additional funding was provided by the San Diego State University Graduate Fellowship and the American Institute of Aeronautics and Astronautics (AIAA) Reuben H. Fleet Scholarship. Computational time for this project was made available through the Department of Defense High Performance Computing Modernization Program (HPCMP) on the Narwhal system at the Navy DSRC, the Warhawk system at the AFRL DSRC, and the Ruth system at the ARL DSRC. The author's acknowledge the use of

## References

- [1] Hesam Abbassi, Farzad Mashayek, and Gustaaf B Jacobs. Shock capturing with entropy-based artificial viscosity for staggered grid discontinuous spectral element method. *Computers & Fluids*, 98:152–163, 2014.
- [2] Mark Ainsworth. Dispersive and dissipative behaviour of high order discontinuous galerkin finite element methods. *Journal of Computational Physics*, 198(1):106–130, 2004.
- [3] John D. Anderson. *Modern Compressible Flow*. McGraw-Hill, 2003.
- [4] M Awasthi, S McCreton, DJ Moreau, and CJ Doolan. Supersonic cylinder wake dynamics. *Journal of Fluid Mechanics*, 945, 2022.
- [5] BS Baldwin and RW MacCormack. Interaction of strong shock wave with turbulent boundary layer. *Proceedings of the Fourth International Conference on Numerical Methods in Fluid Dynamics*, pages 51–56, 2005.
- [6] VA Bashkin, IV Egorov, MV Egorova, and DV Ivanov. Supersonic laminar-turbulent gas flow past a circular cylinder. *Fluid Dynamics*, 35(5):652–662, 2000.
- [7] J. Chai, Z. Pyle, G. Jacobs, N. Sedano, and F. Davoudzadeh. Aerospike flow simulations: From rans to les. *JANNAF*, 2021.
- [8] A Chaudhuri and GB Jacobs. Dynamics of shock wave diffraction over sharp splitter geometry using entropy-based artificial viscosity method. *Shock Waves*, 29:101–115, 2019.
- [9] Arnab Chaudhuri. On shock propagation through double-bend ducts by entropy-generation-based artificial viscosity method. *Entropy*, 21(9):837, 2019.
- [10] Arnab Chaudhuri, Gustaaf B Jacobs, Wai-Sun Don, H Abbassi, and Farzad Mashayek. Explicit discontinuous spectral element method with entropy generation based artificial viscosity for shocked viscous flows. *Journal of Computational Physics*, 332:99–117, 2017.
- [11] Jacqueline H Chen, Brian J Cantwell, and Nagi N Mansour. The effect of mach number on the stability of a plane supersonic wake. *Physics of Fluids A: Fluid Dynamics*, 2(6):984–1004, 1990.
- [12] K Chutkey, M Viji, and SB Verma. Effect of clustering on linear plug nozzle flow field for overexpanded internal jet. *Shock Waves*, 27:623–633, 2017.
- [13] Kiran Chutkey, B Vasudevan, and N Balakrishnan. Flowfield analysis of linear plug nozzle. *Journal of Spacecraft and Rockets*, 49(6):1109–1119, 2012.
- [14] Kiran Chutkey, B Vasudevan, and N Balakrishnan. Analysis of annular plug nozzle flowfield. *Journal of spacecraft and rockets*, 51(2):478–490, 2014.
- [15] Kiran Chutkey, B Vasudevan, and N Balakrishnan. Flow and performance analysis of annular cluster truncated plug nozzle. *Journal of Propulsion and Power*, 32(6):1442–1453, 2016.
- [16] Bernardo Cockburn and Chi-Wang Shu. The runge-kutta discontinuous galerkin method for conservation laws v: multidimensional systems. *Journal of computational physics*, 141(2):199–224, 1998.
- [17] Wai-Sun Don and Rafael Borges. Accuracy of the weighted essentially non-oscillatory conservative finite difference schemes. *Journal of Computational Physics*, 250:347–372, 2013.

- [18] F Ducros, V Ferrand, F Nicoud, C Weber, D Darracq, C Gacherieu, and T Poinso. Large-eddy simulation of the shock/turbulence interaction. *Journal of Computational Physics*, 152(2):517–549, 1999.
- [19] Joseph E Flaherty, Lilia Krivodonova, Jean-Francois Remacle, and Mark S Shephard. Aspects of discontinuous galerkin methods for hyperbolic conservation laws. *Finite Elements in Analysis and Design*, 38(10):889–908, 2002.
- [20] Gregor Gassner and David A Kopriva. A comparison of the dispersion and dissipation errors of gauss and gauss-lobatto discontinuous galerkin spectral element methods. *SIAM Journal on Scientific Computing*, 33(5):2560–2579, 2011.
- [21] Thomas Golliard and Mihai Mihaescu. Computational aeroacoustics for a cold, non-ideally expanded aerospike nozzle. *Journal of Turbomachinery*, 146(2), 2024.
- [22] F Grasso and C Pettinelli. Analysis of laminar near-wake hypersonic flows. *Journal of Spacecraft and Rockets*, 32(6):970–980, 1995.
- [23] G Hagemann, H Immich, and M Terhardt. Flow phenomena in advanced rocket nozzles-the plug nozzle. *AIAA Joint Propulsion Conference and Exhibit*, page 3522, 1998.
- [24] Gerald Hagemann, Hans Immich, and Gennady Dumnov. Critical assessment of the linear plug nozzle concept. *37th AIAA Joint Propulsion Conference and Exhibit*, page 3683, 2001.
- [25] Gerald Hagemann, Hans Immich, Thong Van Nguyen, and Gennady E Dumnov. Advanced rocket nozzles. *Journal of Propulsion and Power*, 14(5):620–634, 1998.
- [26] P Harris and H Fasel. Numerical investigation of the unsteady behavior of supersonic plane wakes. In *29th AIAA, Fluid Dynamics Conference*, page 2974, 1998.
- [27] Sebastian Hennemann, Andrés M Rueda-Ramírez, Florian J Hindenlang, and Gregor J Gassner. A provably entropy stable subcell shock capturing approach for high order split form dg for the compressible euler equations. *Journal of Computational Physics*, 426:109935, 2021.
- [28] L.S. Hesthaven and T. Warburton. Nodel discontinuous-galerkin methods: Algorithms, analysis, and applications. *Numerical Heat Transfer, Part B*, 44:225–251, 2008.
- [29] W Schuyler Hinman and Craig T Johansen. Mechanisms in the hypersonic laminar near wake of a blunt body. *Journal of Fluid Mechanics*, 839:33–75, 2018.
- [30] Fang Q Hu, M Yousuff Hussaini, and Patrick Rasetarinera. An analysis of the discontinuous galerkin method for wave propagation problems. *Journal of Computational Physics*, 151(2):921–946, 1999.
- [31] Takashi Ito, Kozo Fujii, and A Koich Hayashi. Computations of axisymmetric plug-nozzle flowfields: Flow structures and thrust performance. *Journal of Propulsion and Power*, 18(2):254–260, 2002.
- [32] Gustaaf B Jacobs, Jaron Chai, Zachary Pyle, Nils Sedano, and Farhad Davoudzadeh. Aerospike flow simulation: from rans to les. *AIAA Propulsion and Energy Forum, AIAA 2021-3693*, page 3693, 2021.
- [33] Gustaaf B Jacobs, David A Kopriva, and Farzad Mashayek. Validation study of a multidomain spectral code for simulation of turbulent flows. *AIAA journal*, 43(6):1256–1264, 2005.
- [34] Bjoern F Klose, Gustaaf B Jacobs, and David A Kopriva. Assessing standard and kinetic energy conserving volume fluxes in discontinuous galerkin formulations for marginally resolved navier-stokes flows. *Computers & Fluids*, 205:104557, 2020.
- [35] David Kopriva. *Implementing Spectral Methods for Partial Differential Equations*. Springer-Verlag, 2009.

- [36] NASA Marshall Space Flight Center. Linear aerospike engine - propulsion for the x-33 vehicle. *NASA FS-2000-09-174-MSFC*, 2000.
- [37] Thomas J. Mueller and Wayne P. Sule. Base flow characteristics of a linear aerospike nozzle segment. *Journal of Engineering for Industry*, 95(1):353–359, 1973.
- [38] TJ Mueller, Wayne P Sule, and Charles R Hall. Characteristics of separated flow regions within altitude compensating nozzles. *University of Notre Dame*, 1971.
- [39] TJ Muller, WP Sule, AE Fanning, TV Giel, and FL Galanga. Analytical and experimental study of axisymmetric truncated plug nozzle flow fields. *University of Notre Dame*, 1972.
- [40] Prasanth P Nair, Abhilash Suryan, and Heuy Dong Kim. Computational study of performance characteristics for truncated conical aerospike nozzles. *Journal of Thermal Science*, 26:483–489, 2017.
- [41] Prasanth P Nair, Abhilash Suryan, and Heuy Dong Kim. Computational study on flow through truncated conical plug nozzle with base bleed. *Propulsion and Power Research*, 8(2):108–120, 2019.
- [42] Marcello Onofri, M Calabro, G Hagemann, H Immich, P Sacher, Francesco Nasuti, and P Reijasse. Plug nozzles: summary of flow features and engine performance-overview of rto/avt wg 10 subgroup 1. *40th AIAA Aerospace Sciences Meeting and Exhibit*, page 584, 2002.
- [43] Andrew Parsonson. Polaris to begin testing fourth spaceplane demonstrator from september. *European Spaceflight*, Aug. 2023.
- [44] Madeline M Peck, Samuel A Harder, and Jiajia Waters. Comparing discontinuous galerkin shock-capturing techniques applied to inviscid three-dimensional hypersonic flows. *AIAA Journal*, pages 1–15, 2024.
- [45] Sergio Pirozzoli. Numerical methods for high-speed flows. *Annual Review of Fluid Mechanics*, 43(Volume 43, 2011):163–194, 2011.
- [46] Sergio Pirozzoli, Matteo Bernardini, and Francesco Grasso. Direct numerical simulation of transonic shock/boundary layer interaction under conditions of incipient separation. *Journal of Fluid Mechanics*, 657:361–393, 2010.
- [47] Stephen Pope. *Turbulent Flows*. Cambridge University Press, 2000.
- [48] Zachary Pyle, Gustaaf B Jacobs, Nils Sedano, and Farhad Davoudzadeh. Viscous wake effects on the inviscid wall-bounded jet flow over an aerospike nozzle. *AIAA SCITECH 2023 Forum*, page 1469, 2023.
- [49] Saad A Ragab and JL Wu. Linear instabilities in two-dimensional compressible mixing layers. *Physics of Fluids A: Fluid Dynamics*, 1(6):957–966, 1989.
- [50] BE Schmidt and JE Shepherd. Oscillations in cylinder wakes at mach 4. *Journal of Fluid Mechanics*, 785:R3, 2015.
- [51] K Sengupta, GB Jacobs, and F Mashayek. Large-eddy simulation of compressible flows using a spectral multidomain method. *International journal for numerical methods in fluids*, 61(3):311–340, 2009.
- [52] K Sengupta, B Shotorban, GB Jacobs, and F Mashayek. Spectral-based simulations of particle-laden turbulent flows. *International Journal of Multiphase Flow*, 35(9):811–826, 2009.
- [53] Spencer Sherwin. Dispersion analysis of the continuous and discontinuous galerkin formulations. *Discontinuous Galerkin Methods: Theory, Computation and Applications*, pages 425–431, 2000.

- [54] Chi-Wang Shu. High order weighted essentially nonoscillatory schemes for convection dominated problems. *SIAM review*, 51(1):82–126, 2009.
- [55] Jan Sieder-Katzmann, Martin Propst, Ralf H Stark, Dirk Schneider, Stephan General, Martin Tajmar, and Christian Bach. Surface pressure measurement of truncated, linear aerospike nozzles utilising secondary injection for aerodynamic thrust vectoring. *Aerospace*, 11(7):507, 2024.
- [56] Sandeep Soman, Abhilash Suryan, Prasanth P Nair, and Heuy Dong Kim. Numerical analysis of flowfield in linear plug nozzle with base bleed. *Journal of Spacecraft and Rockets*, 58(6):1786–1798, 2021.
- [57] D Stanescu, David A Kopriva, and M Yousuff Hussaini. Dispersion analysis for discontinuous spectral element methods. *Journal of scientific computing*, 15:149–171, 2000.
- [58] David Szondy. German govt awards contract to develop linear aerospike rocket engine. *NewAtlas*, June 2023.
- [59] Christopher KW Tam. Supersonic jet noise. *Annual Review of Fluid Mechanics*, 27:17–43, 1995.
- [60] Christopher KW Tam and Fang Q Hu. On the three families of instability waves of high-speed jets. *Journal of Fluid Mechanics*, 201:447–483, 1989.
- [61] SB Verma and M Viji. Linear-plug flowfield and base pressure development in freestream flow. *Journal of Propulsion and Power*, 27(6):1247–1258, 2011.
- [62] Shashi Verma and Muniyandi Viji. Base pressure characteristics of a linear plug nozzle with freestream effects. *45th AIAA/ASME/SAE/ASEE Joint Propulsion Conference & Exhibit*, page 5148, 2009.
- [63] Shashi Bhushan Verma. Performance characteristics of an annular conical aerospike nozzle with freestream effect. *Journal of Propulsion and Power*, 25(3):783–791, 2009.
- [64] Shashi Bhushan Verma, Ralf Stark, and Oskar Haidn. Relation between shock unsteadiness and the origin of side-loads inside a thrust optimized parabolic rocket nozzle. *Aerospace Science and Technology*, 10(6):474–483, 2006.
- [65] John VonNeumann and Robert D Richtmyer. A method for the numerical calculation of hydrodynamic shocks. *Journal of applied physics*, 21(3):232–237, 1950.
- [66] Mei Zhuang and Paul E Dimotakis. Instability of wake-dominated compressible mixing layers. *Physics of Fluids*, 7(10):2489–2495, 1995.